



**HAL**  
open science

## Heterogeneous electro-Fenton treatment of chemotherapeutic drug busulfan using magnetic nanocomposites as catalyst

Şule Camcıoğlu, Baran Özyurt, Nihal Oturan, David Portehault, Clément  
Trellu, Mehmet Oturan

► **To cite this version:**

Şule Camcıoğlu, Baran Özyurt, Nihal Oturan, David Portehault, Clément Trellu, et al.. Heterogeneous electro-Fenton treatment of chemotherapeutic drug busulfan using magnetic nanocomposites as catalyst. *Chemosphere*, 2023, 341, pp.140129. 10.1016/j.chemosphere.2023.140129 . hal-04246221v2

**HAL Id: hal-04246221**

<https://hal.sorbonne-universite.fr/hal-04246221v2>

Submitted on 17 Oct 2023

**HAL** is a multi-disciplinary open access archive for the deposit and dissemination of scientific research documents, whether they are published or not. The documents may come from teaching and research institutions in France or abroad, or from public or private research centers.

L'archive ouverte pluridisciplinaire **HAL**, est destinée au dépôt et à la diffusion de documents scientifiques de niveau recherche, publiés ou non, émanant des établissements d'enseignement et de recherche français ou étrangers, des laboratoires publics ou privés.

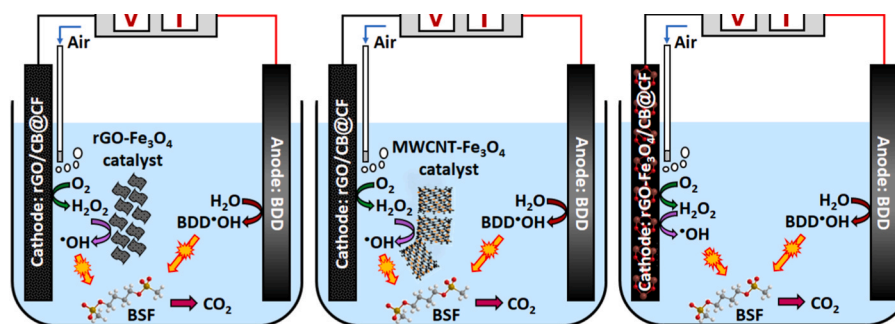
# Heterogeneous electro-Fenton treatment of chemotherapeutic drug busulfan using magnetic nanocomposites as catalyst

Şule Camcıoğlu<sup>a,b,\*\*</sup>, Baran Özyurt<sup>a,b</sup>, Nihal Oturan<sup>b</sup>, David Portehault<sup>c</sup>, Clément Trelu<sup>b</sup>, Mehmet A. Oturan<sup>b,\*</sup>

<sup>a</sup> Ankara University, Faculty of Engineering, Department of Chemical Engineering, 06100, Tandogan, Ankara, Turkey

<sup>b</sup> Université Gustave Eiffel, Laboratoire Géomatériaux et Environnement EA 4508, 77454, Marne-la-Vallée, Cedex 2, France

<sup>c</sup> Sorbonne Université, CNRS, Laboratoire de Chimie de La Matière Condensée de Paris (CMCP), 4 Place Jussieu, Paris, France



The rapid and efficient mineralization of the chemotherapeutic drug busulfan (BSF) as the target pollutant has been investigated for the first time by three different heterogeneous EF systems that were constructed to ensure the continuous electro-generation of  $\text{H}_2\text{O}_2$  and  $\cdot\text{OH}$  consisting of: i) a multifunctional carbon felt (CF) based cathode composed of reduced graphene oxide (rGO), iron oxide nanoparticles and carbon black (CB) ( $\text{rGO-Fe}_3\text{O}_4/\text{CB@CF}$ ), ii) rGO modified cathode ( $\text{rGO/CB@CF}$ ) and rGO supported  $\text{Fe}_3\text{O}_4$  ( $\text{rGO-Fe}_3\text{O}_4$ ) catalyst and iii) rGO modified cathode ( $\text{rGO/CB@CF}$ ) and multi walled carbon nanotube supported  $\text{Fe}_3\text{O}_4$  ( $\text{MWCNT-Fe}_3\text{O}_4$ ) catalyst. The effects of main variables, including the catalyst amount, applied current and initial pH were investigated. Based on the results,  $\text{H}_2\text{O}_2$  was produced by oxygen reduction reaction (ORR) on the liquid-solid interface of both fabricated cathodes.  $\cdot\text{OH}$  was generated by the reaction of  $\text{H}_2\text{O}_2$  with the active site of  $\equiv\text{Fe}^{\text{II}}$  on the surface of the multifunctional cathode and heterogeneous EF catalysts. Utilizing carbon materials with high conductivity, the redox cycling between  $\equiv\text{Fe}^{\text{II}}$  and  $\equiv\text{Fe}^{\text{III}}$  was effectively facilitated and therefore promoted the performance of the process. The results demonstrated almost complete mineralization of BSF through the heterogeneous systems over a wide applicable pH range. According to the reusability and stability tests, multifunctional cathode exhibited outstanding performance after five consecutive cycles which is promising for the efficient mineralization of refractory organic pollutants. Moreover, intermediates products of BSF oxidation were identified and a plausible oxidation pathway was proposed. Therefore, this study demonstrates efficient and stable cathodes and catalysts for the efficient treatment of an anticancer active substance.

## 1. Introduction

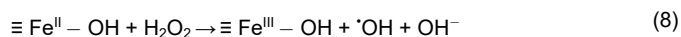
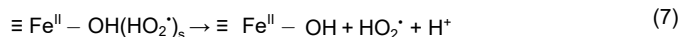
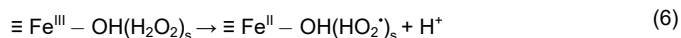
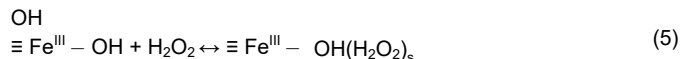
The increasing use of drugs for cancer treatment and their poor metabolism in the human body result in high concentrations of these drugs and/or their metabolites in hospital and municipal wastewaters (Kanjaj et al., 2020; Kulaksız et al., 2022). Effluents from wastewater treatment plants are considered to be the main source of release of these drugs and their metabolites into water resources (Zhang et al., 2013; Ioannou-Ttota and Fatta-Kassinos, 2020; Siedlecka, 2020). Although effluent concentration of chemotherapeutic drugs are generally at  $\text{ng L}^{-1}$  level, they have been shown to have cytotoxic, genotoxic, muta-genic, endocrine disrupting and/or teratogenic effects in aquatic and terrestrial ecosystems (Li et al., 2016; Pieczyńska et al., 2017; Yang et al., 2020a). Recognition of the presence of these drugs has prompted research into potential methods for removing them from water bodies, including activated sludge aerobic bioreactors (Kosjek et al., 2018), photocatalytic degradation (Calza et al., 2014; González-Burciaga et al., 2022), chlorination (Roig et al., 2014), UV/ $\text{H}_2\text{O}_2$ , UV/ $\text{Fe}^{2+}/\text{H}_2\text{O}_2$  and UV/ $\text{TiO}_2$  processes (González-Burciaga et al., 2021; Lutterbeck et al., 2015), ozonation (Li et al., 2016), Fenton reagent (Governo et al., 2017), photo-Fenton (Cavalcante et al., 2013), anodic oxidation (AO) (Barışçı et al., 2018) and EF (Kulaksız et al., 2022; Yang et al., 2019).

As one of the most widely studied electrochemical advanced oxidation processes (EAOPs), electro-Fenton (EF) is considered as a promising method owing to high oxidation/mineralization efficiency against recalcitrant organic pollutants, low cost and simple operating conditions (Camcioglu et al., 2022; Martínez-Huitle et al., 2022). In this process,  $\text{H}_2\text{O}_2$  is electrochemically generated on-site by the two-electron oxygen reduction reaction (ORR) at the carbonaceous cathode (Eq. (1)) (Bar-houmi et al., 2016). Formed  $\text{H}_2\text{O}_2$  is decomposed by the externally added catalyst ( $\text{Fe}^{2+}$ ) promoting the continuous generation of homo-geneous hydroxyl radical ( $\cdot\text{OH}$ ) via Fenton reaction (Eq. (2)) (Zhou et al., 2018).  $\text{Fe}^{2+}$  consumed in Fenton reaction is regenerated electro-chemically of  $\text{Fe}^{3+}$  at the cathode (Eq. (3)) ensuring continuous for-mation of  $\cdot\text{OH}$  (Yang et al., 2019, 2020b).



However, some challenges are encountered during the application of homogeneous EF such as low pH range (pH 2.5–3.5) requirement for optimal process efficiency (Li et al., 2009; Wang et al., 2013; Chen et al., 2015). Further, the catalyst  $\text{Fe}^{2+}$  in homogeneous EF has to be precipitated before discharge, which prevents the reusability and recyclability of the catalyst in continuous processes and also generates a sludge that requires a secondary process to be disposed (Ganiyu et al., 2018; Poza-Nogueiras et al., 2018; Nidheesh et al., 2023b).

To overcome these drawbacks, the heterogeneous EF process, which uses a solid catalyst for the decomposition of  $\text{H}_2\text{O}_2$  to  $\cdot\text{OH}$ , has been developed (Gopinath et al., 2022). Heterogeneous EF process offers so-lutions such as preventing the generation and disposal of iron-rich sludge, widening working pH range, catalyst recovery and reusability by utilizing heterogeneous catalysts and functionalized cathodes with enhanced durability, high conductivity, and large surface area (Ganiyu et al., 2018; Nidheesh et al., 2022). It is widely accepted that heterogeneous EF catalysis may fit the Haber-Weiss mechanism, which is summarized by reactions in Eqs (4)–(9).



When current is applied to the system, partial reduction of  $\equiv\text{Fe}^{\text{III}}-\text{OH}$  to  $\equiv\text{Fe}^{\text{II}}-\text{OH}$  by gaining one electron at the surface of the iron containing heterogeneous catalyst (Eq. (4)) accompanied with generation of  $\text{H}_2\text{O}_2$  in large amounts at the cathode (Eq. (1)) initiates the mechanism (Wang et al., 2013).  $\text{H}_2\text{O}_2$  interacts with the negatively charged catalyst surface, to produce a precursor surface complex ( $\equiv\text{Fe}^{\text{III}}-\text{OH}(\text{H}_2\text{O}_2)_s$ ) representing the surface properties of  $\text{H}_2\text{O}_2$  within the inner and outer surface of the cathode matrix (Eq. (5)). Further, surface  $\text{H}_2\text{O}_2$  complex may be subjected to a reversible ground-state electron transfer from the ligand to metal (Eq. (6)) and the successor complex then would be deactivated through Eq. (7) to form  $\text{HO}_2\cdot$  and  $\equiv\text{Fe}^{\text{II}}-\text{OH}$  (Zhao et al., 2012). It is obvious that the reaction in Eq. (6) is particularly active in alkaline media since the consumption of  $\text{H}^+$  will swiftly change the equilibrium, resulting in the formation of more  $\equiv\text{Fe}^{\text{II}}-\text{OH}$  species (Ganiyu et al., 2018; Zhao et al., 2012). The reduced iron sites ( $\text{Fe}^{\text{II}}-\text{OH}$ ) then again react with  $\text{H}_2\text{O}_2$  (Eq. (8)) to regenerate  $\text{Fe}^{\text{III}}-\text{OH}$  sites and form  $\cdot\text{OH}$  that can oxidize the organic compounds until complete mineralization to  $\text{CO}_2$  and  $\text{H}_2\text{O}$  (Eq. (9)) (Zhao et al., 2012).

Iron oxides are the pillars of nanomaterials used in water treatment due to their natural abundance, and relatively low toxicity towards receiving environments (Rusevova et al., 2012; Xu and Wang, 2012; Ganiyu et al., 2022).  $\text{Fe}_3\text{O}_4$  is the most basic magnetic iron oxide with inverse cubic spinel lattice structure.  $\text{Fe}_3\text{O}_4$  consists of two irons sub-lattice including a tetrahedral coordination filled by  $\text{Fe}^{\text{II}}$  and an octahedral coordination occupied by both  $\text{Fe}^{\text{II}}$  and  $\text{Fe}^{\text{III}}$  (Ganiyu et al., 2022). The co-existence of  $\text{Fe}^{\text{II}}$  and  $\text{Fe}^{\text{III}}$  increases the catalytic decomposition of  $\text{H}_2\text{O}_2$  to form strong oxidizing agent  $\cdot\text{OH}$  (Xue et al., 2009; Gopinath et al., 2022). Although reducing the  $\text{Fe}_3\text{O}_4$  particle size may increase the catalytic activity,  $\text{Fe}_3\text{O}_4$  nanoparticles tend to agglomerate and the surface area is reduced (Gao et al., 2007). To overcome this problem, several studies are carried out on the support of  $\text{Fe}_3\text{O}_4$  nano-particles on solids such as bentonite, alginate, zeolite, alumina, chitosan and carbon nanotube (CNT) (Cleveland et al., 2014; Zhou et al., 2014; Yu et al., 2015), porous carbon-based matrices (Chen et al., 2023), activated carbon (Zhang et al., 2014) and graphene oxide (GO) (Hua et al., 2014; Zubir et al., 2015). CNTs have high chemical and me-chanical stability characteristics, high electrical conductivity, high electroactive surface area (Gopinath et al., 2022). The unique electronic characteristics of these particles have been effectively taken into consideration in the electrochemical process as a method to improve the electron transfer reaction (Sadeghi et al., 2019). Graphene and graphene-based derivatives have demonstrated that they are suitable support materials for improved immobilization of nanomaterials that otherwise would be unstable. Large surface area, enhanced electrical conductivity, and mechanical stability can be listed as the properties of

graphene that make it a suitable choice as a support for the catalysts. Also, the chemical reactivity at the edges of the graphene structure and presence of functional groups facilitate functionalization of graphene making it a potential candidate as a support material for catalysts utilized in heterogeneous Fenton processes (Gopinath et al., 2022). The properties of graphene strongly depend on the reduction process of GO. The reduced graphene oxide (rGO) often contains many defects, such as nanoholes and Stone–Wales defects (heptagon/pentagon bonded carbon atom network). These defects play a crucial role to improve the physical and chemical properties of graphene-based nanomaterials (Le et al., 2015). Accordingly, the electron-transfer ability of GO is restored through the reduction of excess oxygen content present in GO sheets (Divyapriya and Nidheesh, 2020). Loading of iron nanoparticles onto nanostructured carbon materials such as rGO and CNTs not only limit the particle size to the nanoscale but also enhance the chemical stability of the catalyst (Wang et al., 2022). In addition to using as a support, graphene enhances the oxygen transfer as well as generates hydrogen peroxide in EF process (Gopinath et al., 2022). Utilization of a graphene modified cathode and magnetic heterogeneous Fenton catalyst supported on a carbon material (e.g. rGO or CNT) duo can be considered for combining enhanced H<sub>2</sub>O<sub>2</sub> production and easy catalyst recovery and reuse in comparison with conventional homogeneous Fenton catalyst.

In order to eliminate the necessities on the recoverability of the catalyst as well as the limitations of pH range, heterogeneous EF using a graphene modified-Fe<sub>3</sub>O<sub>4</sub> doped cathode can be considered as an alternative approach. The significance of cathode material selection in the EF process depends on the generation of high amounts of H<sub>2</sub>O<sub>2</sub> and the faster regeneration of the iron catalyst, whereas the iron-loaded graphene electrodes could generate <sup>•</sup>OH as major product at the inter-face due to the simultaneous decomposition of electrogenerated H<sub>2</sub>O<sub>2</sub> (Divyapriya and Nidheesh, 2020). GO as a monolayer carbon-based nanomaterial has abundant epoxy groups, hydroxyl groups and carboxyl groups, which provide it more active surface characteristics, higher specific surface area and higher electron mobility. The sp<sup>2</sup> hybrid structure of carbon in GO generates the delocalized π conjugation on the surface of GO layer (Dang et al., 2022). While preparing GO-Fe<sub>3</sub>O<sub>4</sub> composite, the conjugated Fe–O–C bond will form, which will promote the transfer of electrons, thus accelerating the redox cycle of Fe<sup>III</sup>/Fe<sup>II</sup> and further decomposing H<sub>2</sub>O<sub>2</sub> into <sup>•</sup>OH. In addition, Fe<sub>3</sub>O<sub>4</sub> nano-particles within the GO nanosheets can effectively prevent the re-stacking of GO layers and the agglomeration of magnetic nano-particles, contributing to the specific surface area and exposing active sites (Dang et al., 2022). Such a cathode can yield both higher H<sub>2</sub>O<sub>2</sub> production and its conversion to <sup>•</sup>OH efficiency and therefore can be considered as a promising approach (Scaria and Nidheesh, 2022; Martínez-Huitle et al., 2023; Nidheesh et al., 2023a). This Fe<sub>3</sub>O<sub>4</sub> functionalized-graphene supported cathode serves dual purpose as it effectively generates H<sub>2</sub>O<sub>2</sub> and therefore <sup>•</sup>OH via the electrochemical reduction of O<sub>2</sub> and in-situ activation of H<sub>2</sub>O<sub>2</sub>, respectively. Modified carbonaceous cathodes that have carbon black (CB) in their composition provide 2e<sup>-</sup> ORR active sites for in situ production of H<sub>2</sub>O<sub>2</sub> and lower energy consumption per produced H<sub>2</sub>O<sub>2</sub>. High current efficiency of CB containing cathode is attributed to the high electrical conductivity property which is due to the low oxygen content and crystal structure of CB (Dong et al., 2018; Zhang et al., 2019).

In this study, we investigated the mineralization of one of the most used chemotherapy drug, busulfan (BSF, see chemical structure in

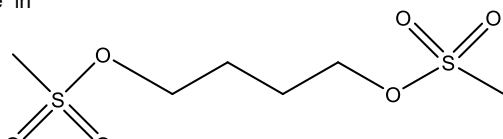


Fig. 1. Chemical structure of Busulfan (BSF).

Fig. 1) (Houot et al., 2013; Skoglund et al., 2013) solutions by the heterogeneous EF processes. To the best of our knowledge, this constitutes the first work on the efficient removal of BSF from contaminated water. We found only one work from Li et al. (2016) in which degradation of eight chemotherapeutic drug was examined by ozonation resulting in lower oxidation kinetics and mineralization rates. Among these chemotherapeutic drugs, BSF was the most recalcitrant to oxidation; only about 20% degradation was achieved with a 1 mg O<sub>3</sub> mg DOC<sup>-1</sup> ozonation dose.

The present study reports fast and complete mineralization after 4 h treatments by means of three heterogeneous EF systems:

- rGO and CB modified carbon felt (CF) cathode (rGO/CB@CF) was fabricated and higher H<sub>2</sub>O<sub>2</sub> production efficiency was obtained in comparison with CF cathode.
- Heterogeneous Fenton process using multi walled carbon nanotube (MWCNT) supported iron oxide (MWCNT-Fe<sub>3</sub>O<sub>4</sub>) and rGO-Fe<sub>3</sub>O<sub>4</sub> catalysts with magnetic properties were fabricated. High efficiencies were achieved for the mineralization of BSF with heterogeneous EF process by using rGO/CB@CF cathode and heterogeneous Fenton catalysts.
- Fe<sub>3</sub>O<sub>4</sub> functionalized-rGO modified CF cathode (rGO-Fe<sub>3</sub>O<sub>4</sub>/CB@CF) was fabricated for generation of H<sub>2</sub>O<sub>2</sub> and its simultaneous conversion to <sup>•</sup>OH to avoid the addition of external catalyst. The application of this multifunctional cathode in heterogeneous EF process exhibited remarkable results in terms of mineralization of BSF. Furthermore, the reaction intermediates formed during the oxidation process, the short-chain carboxylic acids as <sup>-</sup>nal by-products before complete mineralization and mineral end-products were identified using HPLC, GC-MS and IC. These data allowed us to propose a plausible mineralization pathway of BSF by <sup>•</sup>OH generated in the EF process.

## 2. Material and methods

### 2.1. Chemicals

Details of the chemicals used in this study are provided in Supplementary Information file (SI-Text S1).

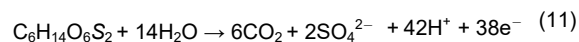
### 2.2. Analytical procedures

The mineralization degree of BSF solutions was determined from their TOC decay measurements on a Shimadzu TOC-V<sub>CSH</sub> analyzer according to the thermal catalytic oxidation principle. Reproducible TOC values are obtained using the non-purgeable organic carbon method with an accuracy of ±2%.

The mineralization current efficiency (MCE) was calculated from TOC values using Eq. (10) at given electrolysis time based on complete electrochemical oxidation of BSF (Brillas et al., 2009; Dos Santos et al., 2020; Dos Santos et al., 2021):

$$\text{MCE}(\%) = \frac{n F V_s \Delta(\text{TOC})_{\text{exp}}}{4.32 \times 10^7 \text{ m l t}} \times 100 \quad (10)$$

Here F is the Faraday constant (96,485 C mol<sup>-1</sup>), V<sub>s</sub> is the solution volume (L), Δ(TOC)<sub>exp</sub> is the experimental TOC decay (mg L<sup>-1</sup>), 4.32 × 10<sup>7</sup> is a conversion factor for homogenization of units, m is the number of carbon atoms of BSF, I is applied current (A), t is the electrolysis time (h). n is the number of electrons consumed per mole of target molecule during its mineralization. The number of electrons are 38 for mineralization of BSF to CO<sub>2</sub> and SO<sub>4</sub><sup>2-</sup> as given in Eq. (11).



The specific energy consumption (EC) per unit TOC mass removed for each experiment was calculated by using Eq. (12) (Márquez et al.,

$$EC(\text{kWh}(\text{g TOC})^{-1}) = \frac{E_{\text{cell}} I t}{V_s \Delta(\text{TOC})_{\text{exp}}} \quad (12)$$

where  $E_{\text{cell}}$  is the mean potential difference of the cell (V). The concentration of  $\text{H}_2\text{O}_2$  was measured via the potassium titanium oxalate method as detailed in SI-Text S2. Short-chain carboxylic acids, inorganic ions and the degradation intermediates formed during treatment were analyzed by HPLC, IC and GC-MS analyses, respectively. The detailed analytical procedures of the methodologies were introduced in SI-Text S2.

### 2.3. Synthesis, preparation and characterization

Synthesis and characterization of GO, rGO,  $\text{Fe}_3\text{O}_4$ , rGO- $\text{Fe}_3\text{O}_4$  and MWCNT- $\text{Fe}_3\text{O}_4$  composites and preparation of modified cathodes are provided in SI-Text S3.

### 2.4. Electrolytic system

Heterogeneous EF experiments were performed in a 100 mL undivided cylindrical glass cell with 80 mL aqueous solution containing 0.1 mM target pollutant and 50 mM  $\text{Na}_2\text{SO}_4$  as supporting electrolyte. BDD ( $16 \text{ cm}^2$ ) and modified electrode ( $8 \text{ cm}^2$ ) were used as anode and cathode, respectively. Experiments were performed under constant current conditions ranging from 100 mA ( $6.25 \text{ mA cm}^{-2}$ ) to 1000 mA ( $62.5 \text{ mA cm}^{-2}$ ). Compressed air bubbling (starting 5 min prior to the experiments) was used to provide saturated oxygen condition in the solution for  $\text{H}_2\text{O}_2$  generation. The pH was measured with a CyberScan pH 1500 pH-meter from Eutech Instruments. The electrochemical cell was powered by a Hameg HM8040 triple DC power supply. Samples were taken at pre-set time intervals to evaluate the concentration for degradation and mineralization.

The  $\text{H}_2\text{O}_2$  electro-generation experiments were performed in an undivided cell (250 mL) in 50 mM  $\text{Na}_2\text{SO}_4$  solution at room temperature and pH = 3. Experiments were performed under 100 mA ( $6.25 \text{ mA cm}^{-2}$ ) constant current electrolysis condition. The unmodified and modified CF cathodes and a Pt sheet of the same geometric area ( $4 \text{ cm} \times 2 \text{ cm}$ ) were used during these experiments.

## 3. Results and discussion

### 3.1. Characterization of GO, rGO, rGO- $\text{Fe}_3\text{O}_4$ , MWCNT and MWCNT- $\text{Fe}_3\text{O}_4$

UV-VIS spectra of GO, rGO and rGO- $\text{Fe}_3\text{O}_4$  is given in Figs. SI-1a. Two characteristic peaks were observed in UV spectra of GO. One of these characteristic peaks at 230 nm was related to  $\pi \rightarrow \pi^*$  transitions of aromatic C-C bonds. The other peak at around 300 nm is attributed to  $n \rightarrow \pi^*$  transitions of C=O bonds (Xu et al., 2011). As seen from the figure, reduction of GO resulted in disappearance of  $n \rightarrow \pi^*$  transition and shifting of  $\pi \rightarrow \pi^*$  transition peak to 267 nm indicating the removal of oxygen containing functional groups from GO and restoration of  $\pi$  network structure (Kavinkumar et al., 2015), hence an extensive reduction process. According to the UV spectra of rGO- $\text{Fe}_3\text{O}_4$ , absorption peak between 350 and 480 nm resulted from the scattering and absorption of UV radiation of magnetic  $\text{Fe}_3\text{O}_4$  nanoparticles (Radoń et al., 2017). The peak due to the  $\pi \rightarrow \pi^*$  transitions of aromatic C-C bonds at  $\sim 270 \text{ nm}$  was diminished. This result suggests that rGO layers may be almost uniformly coated by  $\text{Fe}_3\text{O}_4$  nanoparticles.

The Fourier transform infrared (FTIR) spectra provide information regarding the changes in surface functional group of the samples. The characteristic FTIR functional groups for GO, rGO and rGO- $\text{Fe}_3\text{O}_4$  are presented in Figs. SI-1b. As it is seen from the FTIR spectra of GO, a broad peak at a range of  $3000 \text{ cm}^{-1}$  to  $3700 \text{ cm}^{-1}$  ascribed to the O-H

stretching vibration (Xie et al., 2022). The typical peaks of GO can also be observed at  $1721 \text{ cm}^{-1}$  (C=O carboxylic stretching vibrations),  $1618 \text{ cm}^{-1}$  (C=C stretching vibrations),  $1369 \text{ cm}^{-1}$  (-OH stretching vibrations),  $1221 \text{ cm}^{-1}$  (C-O-C vibrations of epoxy groups),  $1040 \text{ cm}^{-1}$  (C-O stretching vibrations) (Wang et al., 2018). As given in the rGO spectrum, after chemical reduction via hydrazine hydrate, several characteristic peaks of GO were significantly weakened or completely disappeared which implies the elimination of oxygen-containing functional groups during reduction. The weak peak at  $1560 \text{ cm}^{-1}$  which belongs to the skeleton vibration of less-oxidized graphitic materials (Kocijan et al., 2021), C=C, was still existed. Comparison between GO and rGO spectra revealed that partial functional groups in GO had been effectively eliminated by the reduction process. Compared to rGO, the characteristic peak located at  $516 \text{ cm}^{-1}$  in rGO- $\text{Fe}_3\text{O}_4$  nanocomposite is assigned to the Fe-O bond stretching vibration of  $\text{Fe}_3\text{O}_4$  nanoparticles which indicates a C-O-Fe linkage between graphene nanosheets and  $\text{Fe}_3\text{O}_4$  nanoparticles (Es' haghzade et al., 2017; Zhang et al., 2016). The FTIR results confirmed the formation of  $\text{Fe}_3\text{O}_4$  nanoparticles and reduction of some functional groups from GO in rGO- $\text{Fe}_3\text{O}_4$  nanocomposite via the in-situ co-precipitation process.

FTIR spectra of MWCNT,  $\text{Fe}_3\text{O}_4$  and MWCNT- $\text{Fe}_3\text{O}_4$  are given in Figs. SI-1c. The presence of carboxylic groups of MWCNT was confirmed by C=O stretching vibrations at  $1722 \text{ cm}^{-1}$  as well as O-H stretching vibrations at  $3448 \text{ cm}^{-1}$  (Yuan et al., 2016). The characteristic graphite structure peak at  $1573 \text{ cm}^{-1}$  which was assigned to the C=C groups of the MWCNT (Li et al., 2015) is also present in the FTIR spectrum of MWCNT- $\text{Fe}_3\text{O}_4$  nanocomposites (Yuan et al., 2016). The peak located at  $525 \text{ cm}^{-1}$  in MWCNT- $\text{Fe}_3\text{O}_4$  nanocomposite is assigned to the Fe-O bond stretching vibration indicating the presence of  $\text{Fe}_3\text{O}_4$  in the MWCNT- $\text{Fe}_3\text{O}_4$  composite. Compared to MWCNT, the FTIR spectrum of MWCNT- $\text{Fe}_3\text{O}_4$  showed the disappearance of C=O stretching at  $1722 \text{ cm}^{-1}$  which designated the utilization of -COOH of MWCNT by co-precipitation with  $\text{Fe}_3\text{O}_4$  particles. This may also indicate the preparation of the MWCNT- $\text{Fe}_3\text{O}_4$  composite is achieved successfully (Yuan et al., 2016; Zhou et al., 2016).

The crystalline structure of rGO,  $\text{Fe}_3\text{O}_4$  and rGO- $\text{Fe}_3\text{O}_4$  were characterized by XRD (Figs. SI-1d). It is known that GO shows a very sharp characteristic diffraction peak at around  $2\theta = 10.74^\circ$  which corresponds to planar reflection (002) of the GO layers indicates that the distance between the graphene layers (d-spacing) is 0.822 nm (Çıplak et al., 2020). As seen from the XRD results of rGO from Figs. SI-1d, after chemical reduction, the intense peak of GO at around  $2\theta = 10.74^\circ$  completely disappeared and a broad peak occurred at  $2\theta = 24.26^\circ$  with a d-spacing of 0.366 nm which is close to d-spacing value of unoxidized graphite (0.34 nm) (Khan et al., 2019). The decrease in the distance between the graphene layers and a d-spacing value close to the graphite structure, and the disappearance of the characteristic GO peak are the proof for the reduction of GO indicating that the oxygenated functional groups are significantly removed. As seen from the results for  $\text{Fe}_3\text{O}_4$  in Fig. S1d, diffraction peaks at  $2\theta = 30.30^\circ$ ,  $35.53^\circ$ ,  $43.33^\circ$ ,  $53.65^\circ$ ,  $57.18^\circ$ ,  $62.74^\circ$  which are in strong accordance with  $\text{Fe}_3\text{O}_4$  nanoparticles are observed and could be indexed as the characteristic (220), (311), (400), (422), (511) and (440) reflections of the pure cubic spinel crystal structure of  $\text{Fe}_3\text{O}_4$  (Zong et al., 2013). XRD pattern of rGO- $\text{Fe}_3\text{O}_4$  in Fig. S1d shows a presence of mixed phase ( $\text{Fe}_2\text{O}_3$  and  $\text{Fe}_3\text{O}_4$ ), similar to the XRD pattern of standard  $\text{Fe}_2\text{O}_3$  (hematite, JCPDS-04-003-2900) and  $\text{Fe}_3\text{O}_4$  (magnetite, JCPDS-04-007-2718) (Bhuvaneshwari et al., 2014). No obvious typical diffraction peaks of rGO are observed in the XRD spectra of the nanocomposite. This can be attributed to the intense iron oxide peaks, overwhelming the weak rGO peak due to exfoliation (Saipha-neendra et al., 2017).

The morphologies and structures of  $\text{Fe}_3\text{O}_4$ , rGO, rGO- $\text{Fe}_3\text{O}_4$  and MWCNT- $\text{Fe}_3\text{O}_4$  were investigated by TEM. Figs. SI-2a presents a size distribution of nearly spherical shaped  $\text{Fe}_3\text{O}_4$  nanoparticles with particle size less than 10 nm. As can be seen from TEM image, the  $\text{Fe}_3\text{O}_4$  nano-particles are quite agglomerated which may be due to the stronger

magnetic coupling between particles. Figs. SI–2b shows a low magnification TEM image of rGO indicating a typical wrinkled morphology with nanosheets that are less than 5 nm thick. Since the reduction process occurred chemically and caused a change in the structure due to the removal of hydrophilic oxygen-containing functionalities such as hydroxyl, epoxy, and carboxyl groups, rGO presented crumpled and roughed sheets (Geraldino et al., 2020; Wang et al., 2016). The morphological structure of rGO-Fe<sub>3</sub>O<sub>4</sub> was demonstrated by TEM analysis in Figs. SI–2c. It was clear that mostly spherical Fe<sub>3</sub>O<sub>4</sub> nanoparticles with different diameters are distributed on translucent rGO sheets with some agglomeration. Almost no Fe<sub>3</sub>O<sub>4</sub> nanoparticles are found outside of the rGO nanosheets, indicating that rGO-Fe<sub>3</sub>O<sub>4</sub> composite was efficiently synthesized by co-precipitation. Since the Fe<sub>3</sub>O<sub>4</sub> particles are successfully wrapped inside the rGO layers, agglomeration, oxidation, and corrosion by acidic media were prevented and magnetic property was maintained. Microstructure of the MWCNT-Fe<sub>3</sub>O<sub>4</sub> composite is revealed in Figs. SI–2d. MWCNTs have a tubular structure with a small diameter that are entangled with each other. Fe<sub>3</sub>O<sub>4</sub> nanoparticles show a spherical morphology, their sizes are in the range of 10–30 nm and are captured unevenly on the surface of MWCNTs. No Fe<sub>3</sub>O<sub>4</sub> particles are present outside of the MWCNTs, which indicates that the prepared particles are stable in the composite and the interaction between MWCNTs and Fe<sub>3</sub>O<sub>4</sub> nanoparticles are strong. Some agglomerations have observed due to interactions attributed to magnetic properties of Fe<sub>3</sub>O<sub>4</sub> nanoparticles.

### 3.2. Electrochemical characterization of rGO/CB@CF and rGO-Fe<sub>3</sub>O<sub>4</sub>/CB@CF cathodes

LSV (linear sweep voltammetry) and CV (cyclic voltammetry) tests were carried out in the three-electrode cell with the modified cathodes acting as the working electrode in order to explore the effect of modification on the cathode electrochemical activity (Figs. SI–1). LSV was used to quantify ORR for the electrogeneration of H<sub>2</sub>O<sub>2</sub> by measuring the peak current at the working electrode at constant scan rate by varying the potential range. Figs. SI–3a depicts LSV of CF, CB@CF, rGO/CB@CF and rGO-Fe<sub>3</sub>O<sub>4</sub>/CB@CF modified cathodes. The range of potential of LSV was fixed between 0 and –1.5 V to observe the reactions that could occur on the surface of the cathodes. It is clear from the figure that all modified cathodes showed higher current for ORR compared to CF which points out the increase of the catalytic activity towards O<sub>2</sub> reduction and conductivity in the presence of CB and rGO. According to Figs. SI–3a, modification of CF with rGO-Fe<sub>3</sub>O<sub>4</sub> nanocomposite has no significant influence on current response compared with rGO modified cathode. It can be explained by the fact that Fe<sub>3</sub>O<sub>4</sub> nanoparticles were acted as the heterogeneous Fenton catalyst to decompose H<sub>2</sub>O<sub>2</sub> and did not provide ORR active sites in this composite cathode, as indicated by another study (Cui et al., 2020).

[Fe(CN)<sub>6</sub>]<sup>3-</sup>/[Fe(CN)<sub>6</sub>]<sup>4-</sup> redox wave was employed owing to its well-known sensitivity towards the surface properties of carbonaceous electrodes (Wang et al., 2023) to examine the electrochemical surface area of the modified cathodes. As shown in Figs. SI–3b well-defined redox peaks are observed on CVs. The anodic peak centered at ca. 0.4 V ascribed to the oxidation of [Fe(CN)<sub>6</sub>]<sup>4-</sup> and the cathodic peak at ca. 0.175 V points out the reduction of [Fe(CN)<sub>6</sub>]<sup>3-</sup> (Zhai et al., 2019). Compared with CF, 2.30-fold increase of the peak current was observed with rGO/CB@CF which demonstrates much more active sites, since the higher electroactive surface area of electrode is, the higher increase of the peak current (Le et al., 2015). According to Eq. (S2), electrochemical surface areas of rGO/CB@CF and rGO-Fe<sub>3</sub>O<sub>4</sub>/CB@CF were found as 27.22 cm<sup>2</sup> and 25.62 cm<sup>2</sup>, respectively while it was 11.67 cm<sup>2</sup> for CF. The CV curve of the rGO-Fe<sub>3</sub>O<sub>4</sub>/CB@CF was obtained very close to rGO/CB@CF which is consistent with the results of LSV test. It is clear that modification increases the electroactive surface of CF indicating that much more active sites are available for electrochemical reaction due to the more facile electron and mass transfers (Zhai et al., 2019).

Electrochemical H<sub>2</sub>O<sub>2</sub> generation performance and TOC removal rate of different cathodes are given in Fig. 2. Compared with the unmodified CF (Fig. 2a), H<sub>2</sub>O<sub>2</sub> production increased 9.6-fold for CB@CF and 23.4-fold for rGO/CB@CF due to the improved mass transfer kinetics of oxygen and enhanced electrocatalytic properties. H<sub>2</sub>O<sub>2</sub> generation rate of rGO/CB@CF was obtained as 10.96 mg h<sup>-1</sup> cm<sup>-2</sup> (10.32 mmol L<sup>-1</sup> h<sup>-1</sup>), which was significantly higher than the rate yielded by CB@CF as 4.48 mg h<sup>-1</sup> cm<sup>-2</sup> (4.22 mmol L<sup>-1</sup> h<sup>-1</sup>). The introduction of CB and rGO on the cathode not only accelerated the rates of electrons transfer without changing the mechanism of ORR but also increased the cathode surface hydrophilicity to promote mass transfer between the active sites of the cathode and O<sub>2</sub> in the solution for more efficient H<sub>2</sub>O<sub>2</sub> electro-generation (Du et al., 2021; Le et al., 2015; Tao et al., 2021). Furthermore, the electroactive surface of the cathode was also improved, which increased the active sites on the cathode for ORR (Yang et al., 2017). Addition of PTFE to CB@CF and rGO/CB@CF cathodes aids the formation of gas–solid–liquid three-phase interfaces similar to gas diffusion electrode; this thus enabling the effective use of both dissolved and gaseous O<sub>2</sub> (Cui et al., 2021). When the cathode is modified hydrophobic partially and hydrophilic partially, the O<sub>2</sub> bubble could be confined to the hydrophobic location and enables the formation of a gas–liquid–solid interface (Sheng et al., 2011). The hydrophilic location functions as active sites for H<sub>2</sub>O<sub>2</sub> production by utilizing the neighboring O<sub>2</sub>. The advantage of hydrophilicity–hydrophobicity regulation is that the more efficient H<sub>2</sub>O<sub>2</sub> production could be enabled by using simple electrode structures (Zhou et al., 2021). The higher H<sub>2</sub>O<sub>2</sub> production performance of rGO/CB@CF over CB@CF can be explained by contribution of above mentioned factors. H<sub>2</sub>O<sub>2</sub> accumulation of rGO–Fe<sub>3</sub>O<sub>4</sub>/CB@CF was found to be decreased in comparison to CB@CF and rGO/CB@CF which means a large amount of electrogenerated H<sub>2</sub>O<sub>2</sub> decomposed onsite into <sup>•</sup>OH in consequence of Fe<sub>3</sub>O<sub>4</sub> activation (Cui et al., 2021). Heterogeneous EF performance of the modified cathodes was also determined by comparing TOC mineralization rates (Fig. 2b). Mineralization of BSF within 1 h reached 98.2% with rGO/CB@CF cathode and MWCNT-Fe<sub>3</sub>O<sub>4</sub> catalyst system and 99.1% with rGO–Fe<sub>3</sub>O<sub>4</sub>/CB@CF cathode, which was higher than that of CF cathode (81.2%). TOC removal rate of CF cathode was found as the lowest due to the fact that it has a weaker performance of ORR to generate H<sub>2</sub>O<sub>2</sub>. Modification of the cathodes by rGO contributed to the higher H<sub>2</sub>O<sub>2</sub> accumulation (Xie et al., 2022) and thus higher TOC mineralization yield. Onsite decomposition of H<sub>2</sub>O<sub>2</sub> into <sup>•</sup>OH on the multifunctional rGO-Fe<sub>3</sub>O<sub>4</sub>/CB@CF cathode was also confirmed by obtaining a very close mineralization yield in comparison with the rGO/CB@CF cathode and MWCNT-Fe<sub>3</sub>O<sub>4</sub> catalyst system.

### 3.4. Heterogeneous EF treatment of BSF

#### 3.4.1. The effect of catalyst dosage on mineralization rate of BSF

It is well known that catalyst concentration plays a fundamental role in the efficiency of heterogeneous EF process, since it controls the rate of <sup>•</sup>OH production. To determine the optimal value of the heterogeneous catalyst concentration, BSF solutions were treated by employing MWCNT-Fe<sub>3</sub>O<sub>4</sub> and rGO-Fe<sub>3</sub>O<sub>4</sub> catalysts in the range of 0.2–1.0 g L<sup>-1</sup> at 100 mA and the results were shown in Fig. 3a–b. A much slower mineralization was observed during AO (0 g L<sup>-1</sup>) with BDD anode because of the mass transport limitation of BSF from the bulk to the electrode surface (Fig. 3a–b). Faster mineralization of BSF in heterogeneous EF processes are ascribed to a much more favorable mass transport conditions for reactions of BSF with <sup>•</sup>OH formed in the bulk, compared to reaction with BDD (<sup>•</sup>OH) generated at the anode surface. Maximum mineralization efficiency was achieved with 0.2 g L<sup>-1</sup> of MWCNT-Fe<sub>3</sub>O<sub>4</sub> and rGO-Fe<sub>3</sub>O<sub>4</sub> resulting in a TOC removal of 89.4% and 96.9%, respectively (Fig. 2a and b). It can be seen that mineralization rate of BSF is decreased with increasing catalyst concentration from 0.2

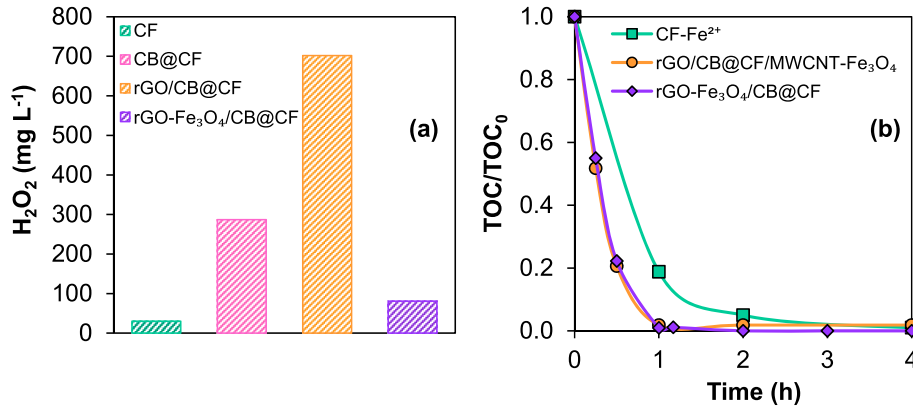


**Fig. 2.** Electrochemical generation of H<sub>2</sub>O<sub>2</sub> (a) and TOC removal rate (b) using different cathodes at pH = 3 in 50 mM Na<sub>2</sub>SO<sub>4</sub> solution. (a): t = 2 h, V = 250 mL, I = 100 mA (6.25 mA cm<sup>-2</sup>). (b): [BSF] = 0.1 mM, V = 80 mL, I = 500 mA (31.25 mA cm<sup>-2</sup>). For CF (homogeneous EF): [Fe<sup>2+</sup>] = 0.1 mM. For heterogeneous EF with rGO/CB@CF cathode/MWCNT-Fe<sub>3</sub>O<sub>4</sub> catalyst system: [MWCNT-Fe<sub>3</sub>O<sub>4</sub> catalyst] = 0.5 g L<sup>-1</sup>).

to 1 g L<sup>-1</sup>. The lowest efficiency was observed at the highest catalyst load (1 g L<sup>-1</sup>) as 57.05% for MWCNT-Fe<sub>3</sub>O<sub>4</sub>, whereas it was 0.5 g L<sup>-1</sup> for rGO-Fe<sub>3</sub>O<sub>4</sub> (86.5%). It is reported that the amount of catalyst has a direct effect on the reaction kinetics, since Fe is the catalyst for decomposition of H<sub>2</sub>O<sub>2</sub> to form <sup>•</sup>OH. However, when iron oxide is in excess, the scavenging effect of Fe<sup>2+</sup> is enhanced and results in consumption of <sup>•</sup>OH through Eq. (13) (Lin et al., 2017; Sadeghi et al., 2019; Chen et al., 2016; Geraldino et al., 2020).

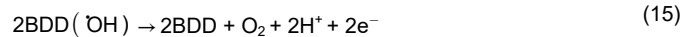
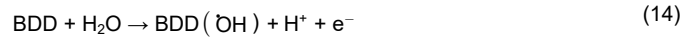


Therefore, 0.2 g L<sup>-1</sup> catalyst dosage was chosen as the optimum value for further experiments, considering the mineralization efficiency and catalyst cost.

### 3.4.2. The effect of applied current on mineralization rate of BSF

In order to explore the performance of heterogeneous EF process for complete mineralization of BSF solution, TOC removal experiments were conducted and results are depicted in Fig. 3c–e. Current density is the driving force for electron transfer between the surface of electrodes and the bulk aqueous solution, which controls the amount of H<sub>2</sub>O<sub>2</sub> and therefore <sup>•</sup>OH generation. Fig. 3c shows that BSF is completely removed at 1 h of electrolysis at applied current values of 500 mA (31.25 mA cm<sup>-2</sup>) and 1000 mA (62.5 mA cm<sup>-2</sup>) in rGO-Fe<sub>3</sub>O<sub>4</sub>/CB@CF cathode system, while TOC removal efficiency was 92.3% at applied current of 100 mA (6.25 mA cm<sup>-2</sup>) at the end of 4 h. When rGO/CB@CF cathode/ MWCNT-Fe<sub>3</sub>O<sub>4</sub> catalyst system was used, complete mineralization of BSF was achieved at 500 mA (31.25 mA cm<sup>-2</sup>) and 1000 mA (62.5 mA cm<sup>-2</sup>) at 1 h of electrolysis, whereas mineralization rate reached 81.7% and 95.5% at 100 mA (6.25 mA cm<sup>-2</sup>) and 300 mA (18.75 mA cm<sup>-2</sup>), respectively after 2 h of treatment. For rGO/CB@CF cathode/rGO-Fe<sub>3</sub>O<sub>4</sub> catalyst system, TOC mineralization efficiency was increased from 81.3% to 97.3% by increasing current density from 100 to 500 mA (31.25 mA cm<sup>-2</sup>) after 2 h of electrolysis time. Increasing the applied current further to 1000 mA (62.5 mA cm<sup>-2</sup>) did not have a considerable effect on the mineralization rate. Considering the results for three systems, TOC removal efficiency increased regularly with increasing applied current density up to 500 mA (31.25 mA cm<sup>-2</sup>) owing to the promotion of heterogeneous EF in three ways. First, the electro-regeneration of the ≡Fe<sup>II</sup> catalyst increases at high currents due to the cathodic reduction of ≡Fe<sup>III</sup> (Eq. (4)), resulting in an increase in the reaction rate. Secondly, AO (Eq. (14)) increases with applied current and creates a synergy with the catalyst regeneration at the cathode enhancing EF mineralization of organics in water. Finally, the in situ electro-generation of H<sub>2</sub>O<sub>2</sub> (Eq. (1)) by the cathodic reduction of oxygen is dependent on the applied current (Muzenda and Arotiba, 2022). However, by increasing the applied current up to 1000 mA (62.5 mA

cm<sup>-2</sup>), no significant improvement was observed in BSF mineralization due to the increased rate of side reactions that inhibit the formation of <sup>•</sup>OH or increase its consumption (Burgos-Castillo et al., 2018; Nidheesh et al., 2023b). The most significant side reactions are evolution of O<sub>2</sub> on the anode surface (Eq. (15)) and in the bulk (Eq. (16)) which slows down the AO rate and the evolution of H<sub>2</sub> at the cathode (Eq. (17)), which is in competition with the ORR. (Brillas et al., 2009; Sirés et al., 2014; Berhe et al., 2022; Moratalla et al., 2022).



Mineralization experiments were also evaluated to estimate the oxidizing power of the heterogeneous EF process with different systems. The degree of TOC removal was the highest for rGO-Fe<sub>3</sub>O<sub>4</sub>/CB@CF cathode system, except for 100 mA current (6.25 mA cm<sup>-2</sup>), which finally reached 92.3% mineralization efficiency at the end of 4 h. Results indicate the ability of Fe<sub>3</sub>O<sub>4</sub> functionalized-carbonaceous material (rGO) supported CF cathode to serve dual purpose of electrode as well as the catalyst source in heterogeneous EF system. This behavior was associated with the synergistic structural and functional effects of the combination of rGO and Fe<sub>3</sub>O<sub>4</sub> nanoparticles as a potential strategy to improve the rate of Fe<sup>3+</sup> cathodic reduction by the enhancement of electron transfer through catalytic effects, such as creation of active sites in carbon based materials (Deng et al., 2023). Firstly, the high surface area of rGO promotes the dispersion of Fe<sub>3</sub>O<sub>4</sub> nanoparticles, thereby markedly reducing aggregation and favoring mass transfer of reactants toward the active sites. Secondly, there are strong interactions between Fe<sub>3</sub>O<sub>4</sub> nanoparticles and rGO via Fe–O–C bonds, which favors transfer of electrons between the nanoparticles and the conductive rGO sheets. Thirdly, the regeneration of ferrous ions is facilitated that helps electron transport to speed up the redox cycle between the active sites (≡Fe<sup>II</sup>/≡Fe<sup>III</sup>) (Munoz et al., 2015; Zubir et al., 2014).

In this study, GO was prepared through the Hummer's method, which is characterized with the highly reactive oxygen functional groups. These abundant oxygen functional groups of GO exhibit high charge-transfer resistance. Therefore, the ability of GO for transferring the electrons is restored through the reduction of excess oxygen content. The reduction of oxygen was done through a chemical pathway. During the reduction of GO, major oxygen functionalities which introduce the charge-transfer resistance are reduced. Only the stable oxygen functionalities (O–H, C–O, and C=O) that are contributed by phenol,

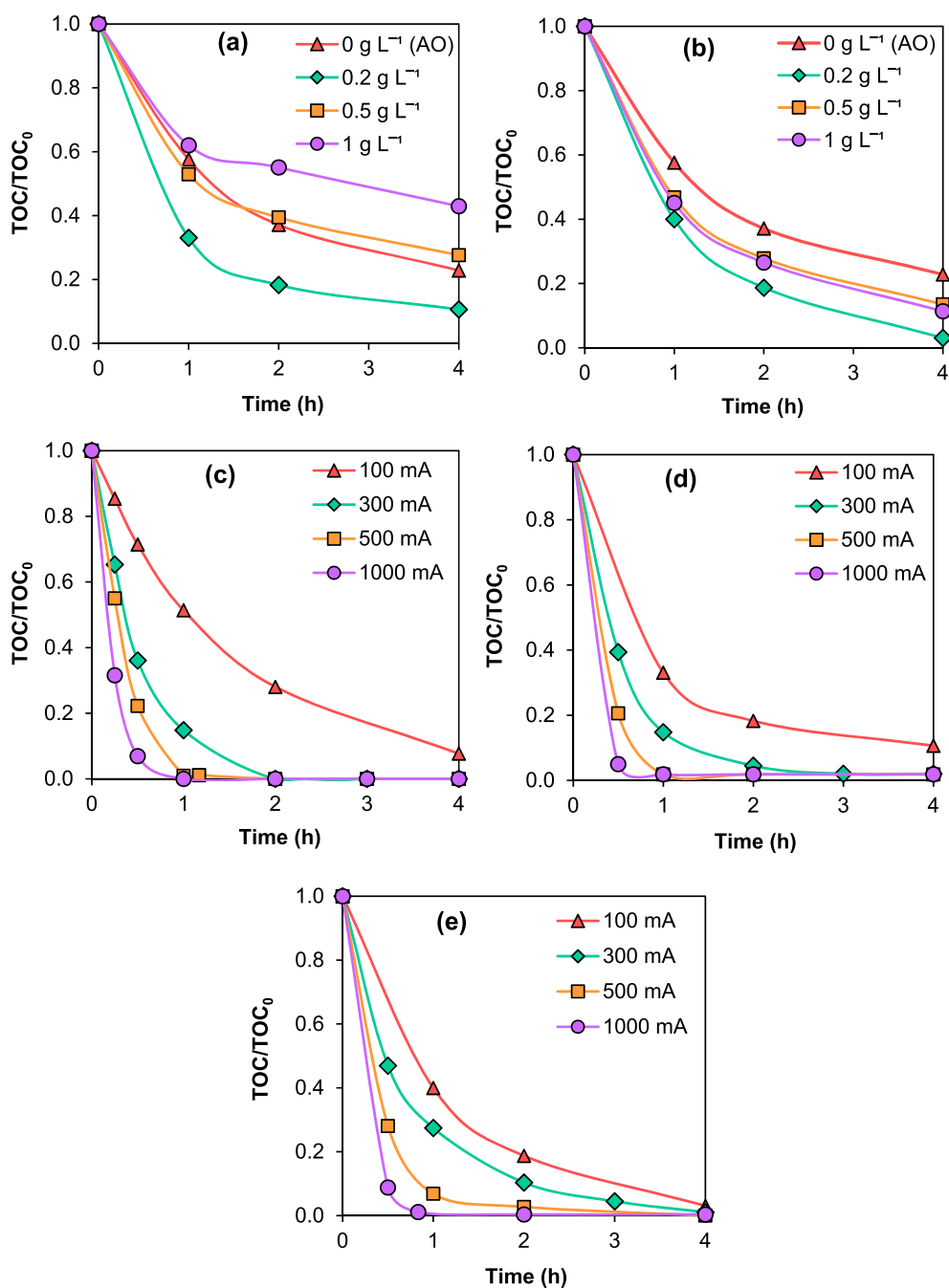


**Fig. 3.** TOC decay of 0.1 mM BSF in 50 mM  $\text{Na}_2\text{SO}_4$  solution as a function of operating parameters: catalyst dosage to rGO/CB@CF cathode/MWCNT- $\text{Fe}_3\text{O}_4$  catalyst system at  $I = 100$  mA ( $6.25 \text{ mA cm}^{-2}$ ) (a) and to rGO/CB@CF cathode/rGO- $\text{Fe}_3\text{O}_4$  catalyst system at  $I = 100$  mA ( $6.25 \text{ mA cm}^{-2}$ ) (b); applied current to rGO- $\text{Fe}_3\text{O}_4$ /CB@CF cathode system (c) and to rGO/CB@CF cathode/MWCNT- $\text{Fe}_3\text{O}_4$  catalyst system at  $[\text{MWCNT-Fe}_3\text{O}_4 \text{ catalyst}] = 0.2 \text{ g L}^{-1}$  (d); applied current to rGO/CB@CF cathode/rGO- $\text{Fe}_3\text{O}_4$  catalyst system at  $[\text{rGO-Fe}_3\text{O}_4 \text{ catalyst}] = 0.2 \text{ g L}^{-1}$  (e). pH = 3, V = 80 mL, BDD anode.

quinone, ether, and carbonyl groups remain. Oxygen-based functional groups present in the carbonaceous cathode act as the active sites to adsorb the dissolved oxygen molecules and convert them to  $\text{H}_2\text{O}_2$  through a two-electron-based ORR (Divyapriya and Nidheesh, 2020). rGO- $\text{Fe}_3\text{O}_4$  and MWCNT- $\text{Fe}_3\text{O}_4$  catalyst systems utilize rGO/CB@CF cathode that could produce high quantities of  $\text{H}_2\text{O}_2$ . Compared to the rGO- $\text{Fe}_3\text{O}_4$  catalyst, MWCNT- $\text{Fe}_3\text{O}_4$  catalyst seems to provide a slight improvement in TOC removal efficiency. This slight difference may arise from the catalytic decomposition of  $\text{H}_2\text{O}_2$  to  $\cdot\text{OH}$  either by homogeneous  $\text{Fe}^{3+}/\text{Fe}^{2+}$  cycle due to the leaching of iron and surface  $\equiv\text{Fe}^{\text{III}}/\equiv\text{Fe}^{\text{II}}$  redox couple (Ganiyu et al., 2018; Görmez et al., 2019). Improved performance with the MWCNT- $\text{Fe}_3\text{O}_4$  catalyst system might be attributed to the enhanced transformation efficiency of  $\equiv\text{Fe}^{\text{III}}$  to  $\equiv\text{Fe}^{\text{II}}$  as follows: Owing to the  $\pi$ -conjugative structure of MWCNT, the BSF molecules were adsorbed on the surface of MWCNT through  $\pi$ - $\pi$

electrostatic interaction, which can be easily attacked by the  $\cdot\text{OH}$  generated on the immobilized Fe-ions (Hu et al., 2011). Furthermore, MWCNT have nonplanar  $\text{sp}^2$ -hybridized framework. In the case of MWCNT- $\text{Fe}_3\text{O}_4$ , iron is bound to MWCNT which leads to a partial electron transfer to the graphite due to the d orbital of Fe hybridizing strongly with the  $p_z$  orbital of the graphitic carbon (Deng et al., 2012). Hence,  $\equiv\text{Fe}^{\text{III}}$  facilitates the reduction by  $\text{H}_2\text{O}_2$  to accelerate circulation of  $\equiv\text{Fe}^{\text{II}}/\equiv\text{Fe}^{\text{III}}$  since the electron density of iron transfers from the iron center. Eventually, the  $\text{H}_2\text{O}_2$  activating ability and catalytic activity are improved (Tang and Wang, 2017).

The TOC removal curves obtained at 1000 mA ( $62.5 \text{ mA cm}^{-2}$ ) for the three systems are almost identical to those obtained at 500 mA ( $31.25 \text{ mA cm}^{-2}$ ), underlying that no enhancement in mineralization efficiency observed for currents above 500 mA ( $31.25 \text{ mA cm}^{-2}$ ) due to the wasting Eqs.(18)–(20) that hinder the increase in  $\text{H}_2\text{O}_2$  production



such as 4-electron reduction of O<sub>2</sub> (Eq. (18)), reduction of H<sub>2</sub>O<sub>2</sub> at the cathode (Eq. (19)) and dimerization of  $\cdot$ OH (Eq. (20)) (Olvera-Vargas et al., 2022; Sopaj et al., 2020).



Results highlight the contribution of BDD ( $\cdot$ OH) on AO to the mineralization of BSF solution is important due to its large mineralization power as already reported (Sopaj et al., 2016). When using BDD anode, it is considered that both  $\cdot$ OH (predominant oxidant) and sulfate radical (SO<sub>4</sub><sup>•-</sup>) are generated and participated in the oxidation of the organics. A major challenge of wastewater treatment by electrochemically generated sulfate reactive species using BDD electrode is that, high concentration of SO<sub>4</sub><sup>2-</sup> ions are usually require as precursor for the generation of sulfate reactive species. In fact, electrochemical oxidation processes are performed in  $\geq 50$  mM SO<sub>4</sub><sup>2-</sup> medium, which indicate high chemical is required for successful wastewater treatment by electro-chemically generated sulfate reactive species (Ganiyu and Martí-nez-Huitile, 2019). In this study, 50 mM Na<sub>2</sub>SO<sub>4</sub> was used as the electrolyte which indicates that the formation of SO<sub>4</sub><sup>•-</sup> at such a low concentration is a low prospect.

#### 3.4.3. Efficiency of different systems on mineralization of BSF solution

The results presented in Figs. SI-4 are obtained from corresponding mineralization data of Fig. 3c-e. Figs. SI-4 depicts the evolution of MCE for applied current values ranging from 100 mA (6.25 mA cm<sup>-2</sup>) to 1000 mA (62.5 mA cm<sup>-2</sup>) during the mineralization process of BSF solution. As seen from this figure, MCE values are relatively high for three systems at low currents and early stage of electrolysis which is an indicator of rapid mineralization of organic intermediates by the action of  $\cdot$ OH/BDD ( $\cdot$ OH). MCE values then kept diminishing with increasing current until the end of 4 h treatment. This can be explained by the production of hardly oxidizable by-products, such as short-chain carboxylic acids, and the reduction of organic matter concentration in the solution resulting in mass transport limitation to BDD anode (Yang et al., 2020b). On the other hand, low MCE values for high currents can be related to acceleration of parasitic reactions consuming  $\cdot$ OH, mainly oxidation of BDD ( $\cdot$ OH) to O<sub>2</sub> at the anode surface (Eq. (15)), dimerization of  $\cdot$ OH to H<sub>2</sub>O<sub>2</sub> (Eq. (20)), as well as the wasting of  $\cdot$ OH by Fe<sup>2+</sup> (Eq. (13)) and H<sub>2</sub>O<sub>2</sub> (Eq. (21)) (Barhoumi et al., 2017), decomposition of H<sub>2</sub>O<sub>2</sub> to H<sub>2</sub>O at the cathode surface (Eq. (19)) and particularly the evolution of H<sub>2</sub> at the cathode (Eq. (17)) which competes with the formation of H<sub>2</sub>O<sub>2</sub> (Eq. (1)) as well as the evolution of O<sub>2</sub> at the anode (Eq. (16)) (Lin et al., 2017). At higher organic matter concentration, when oxidizing radicals can more easily encounter organic molecules, the role of parasitic reactions is less relevant (Brillas and Martínez-Huitile, 2015; Coria et al., 2018).



In the EAOPs, high currents could generally improve the mineralization efficiency but at the same time lead to low MCE because of the side and wasting reactions in addition of quick formation of hardly oxidizable intermediates such as carboxylic acids (García-Segura and Brillas, 2011; Yang et al., 2020a). Therefore, EC as one of the important parameters will be taken into consideration for comparison of mineralization performance. As can be seen from Figs. SI-5, decay of MCE is generally expected to be associated with an increase in EC per unit mass of TOC (Feng et al., 2023). The results given in Figs. SI-5 show that higher currents and longer electrolysis times result in high EC. This highlights that a compromise between high efficiency and low cost is required. Taking into account of the mineralization rate and energy efficiency, the current value of 500 mA (31.25 mA cm<sup>-2</sup>) seems to be the best condition for the three systems as total mineralization can be

reached at a medium cost. EC results showed that systems with cathode and catalyst completely prepared with rGO had relatively lower EC due to the enhanced electrical conductivity of rGO.

#### 3.4.4. The effect of initial pH on mineralization rate of BSF

The most important superiority of heterogeneous EF over its homogeneous equivalent, which performs significantly low efficiency when working outside the pH range 2.5–3.5, is that it can be operated over a wide pH range (Hien et al., 2022). The effect of pH (3–9) on the mineralization performance of the as-prepared cathodes and catalysts was investigated (Figs. SI-6). Heterogeneous EF treatment of all the three systems showed complete mineralization of BSF solutions over the pH range studied at applied current of 500 mA (31.25 mA cm<sup>-2</sup>) proving that the reaction is not limited to a narrow pH working window during heterogeneous EF process where the homogeneous EF process would have completely inhibited by the precipitation of the iron catalyst as iron hydroxide. The results implied notable performance in mineralization of BSF using dual functioning cathode (rGO-Fe<sub>3</sub>O<sub>4</sub>/CB@CF) and paired systems (rGO/CB@CF cathode/MWCNT-Fe<sub>3</sub>O<sub>4</sub> catalyst and rGO/CB@CF cathode/rGO-Fe<sub>3</sub>O<sub>4</sub> catalyst) over a wide range of pH that points out the pH-independent characteristics of the configurations. This can be explained by the fact that Fe<sub>3</sub>O<sub>4</sub> nanoparticles loaded on rGO or MWCNT have high stability at high pH values since they are immobilized in a carbonaceous material and formation of  $\cdot$ OH from H<sub>2</sub>O<sub>2</sub> occurs at the surface of Fe<sub>3</sub>O<sub>4</sub>. Enlargement of the working pH range for the multifunctional cathode can be attributed to the direct occurrence of H<sub>2</sub>O<sub>2</sub> electrogeneration and the oxidation processes at the cathode surface (Brillas, 2022).

$\equiv\text{Fe}^{\text{III}}$  facilitates the reduction by H<sub>2</sub>O<sub>2</sub> to accelerate the cycle between  $\equiv\text{Fe}^{\text{III}}$  and  $\equiv\text{Fe}^{\text{II}}$  because the electron density of iron transfers from the iron center (Deng et al., 2012; Görmez et al., 2019). Therefore, enhanced catalytic activity is ascribed to synergetic effect arising from Fe<sub>3</sub>O<sub>4</sub> and rGO - MWCNT hybrid structure. It is thought that since Fe<sub>3</sub>O<sub>4</sub> nanoparticles are present in the pore/interlayer space of MWCNT/rGO, the catalyst was kept stable without any iron hydroxide formation in alkaline solution, which enables a wider working pH range.

#### 3.5. Identification and evolution of carboxylic acids and inorganic ions with heterogeneous EF process

Treatment of organic pollutants by electrochemical advanced oxidation processes generally leads to the generation of short-chain carboxylic acids as the last intermediates of the mineralization process before transformation into CO<sub>2</sub>, H<sub>2</sub>O and inorganic ions (Camcioglu et al., 2022; Mbaye et al., 2022). Formation and evolution of different carboxylic acids generated during the oxidative degradation of BSF by heterogeneous EF process with rGO-Fe<sub>3</sub>O<sub>4</sub>/CB@CF cathode is given in Fig. 4a. Four distinctive and well-defined peaks corresponding to oxalic, glyoxylic, pyruvic and formic acids were shown on the HPLC chromatograms at retention time of 6.64, 9.17, 11.28 and 13.55 min, and quantified with different accumulation trends. Oxalic acid is generated from the beginning of the process and increased gradually until reaching the maximum peak concentration (0.088 mM) at 120 min. Then, its concentration progressively decreased but not completely disappeared at the end of 6 h treatment, since this acid is known to be resistant to oxidation by  $\cdot$ OH and responsible for the residual TOC at the end of treatment (Diaw et al., 2020). Glyoxylic acid reached its maximum concentration of 0.042 mM after 90 min of electrolysis and then completely mineralized at 300 min. For formic acid, maximum concentration of 0.023 mM was attained after 20 min electrolysis and this acid disappeared after 120 min. Pyruvic acid was only detected at trace amounts along electrolysis.

Inorganic ion formed during the mineralization of 0.1 mM BSF solution were identified and quantified by IC. BSF contains two S atoms in its initial structure which expected to be mineralized into inorganic ion SO<sub>4</sub><sup>2-</sup> upon bond cleavage of BSF molecule. The evolution of SO<sub>4</sub><sup>2-</sup> ion

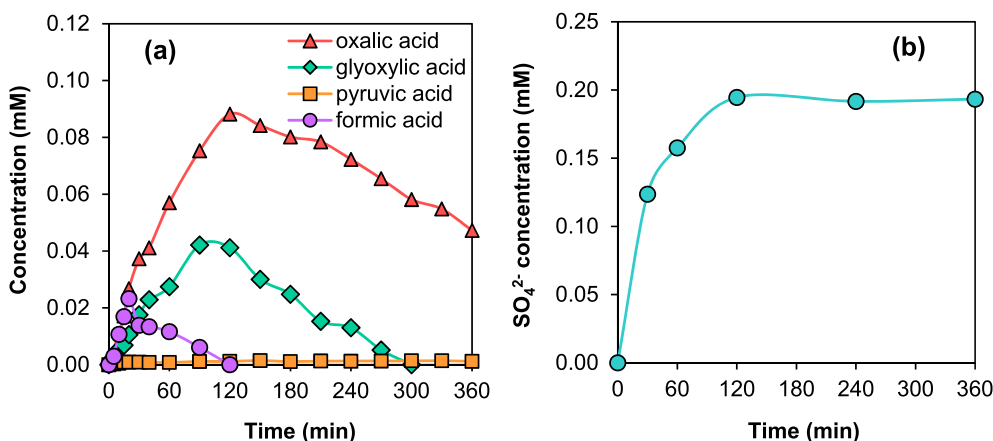


**Fig. 4.** Evolution of short-chain carboxylic acids (a) and sulfate concentration (b) during heterogeneous EF treatment of 0.1 mM BSF solution ( $V = 80$  mL) with BDD anode and rGO-Fe<sub>3</sub>O<sub>4</sub>/CB@CF cathode at pH = 3. Applied current was 100 mA ( $6.25 \text{ mA cm}^{-2}$ ) for carboxylic acids whereas it was 300 mA ( $18.75 \text{ mA cm}^{-2}$ ) for inorganic ion. The supporting electrolyte was 50 mM Na<sub>2</sub>SO<sub>4</sub> for carboxylic acids while it was 15 mM NaClO<sub>4</sub> for inorganic ions to avoid the interference of SO<sub>4</sub><sup>2-</sup> ions on analysis.

generated during heterogeneous EF with rGO-Fe<sub>3</sub>O<sub>4</sub>/CB@CF cathode was presented in Fig. 4b. The concentration of SO<sub>4</sub><sup>2-</sup> increased rapidly and accumulated until reaching the maximum value at 120 min indicating that the S bridge in the BSF molecule is a high reacting site for the attack of <sup>•</sup>OH (Oturán et al., 2017). SO<sub>4</sub><sup>2-</sup> concentration remained constant throughout the electrolysis (0.193 mM) corresponding to 97% of initial S atom.

### 3.6. Reaction pathway for the mineralization of BSF

Several organic by-products formed during EF treatment of BSF solution were identified by GC-MS and HPLC. Tables SI-1 summarizes the characteristics of the intermediates formed from oxidation of BSF. Based on these detected species, a reaction pathway (Figs. SI-7) is proposed for the mineralization of BSF by <sup>•</sup>OH. The intermediates I to IV were identified thanks to the fragmentation analysis of GC-MS spectrum while the intermediates V to VIII were identified by ion-exclusion HPLC analysis. The proposed pathway starts by the attack of <sup>•</sup>OH on BSF leading to oxidative cleavage into molecules I and II. Compound III was resulted from hydroxylation of compound I, whereas compound IV was formed by the cyclization of compound I via intramolecular alkylation (Feit and Rastrup-Andersen, 1973; Myers et al., 2017). The mineralization experiments led also to the formation of carboxylic acids (compounds V to VIII) (Fig. 4a) and SO<sub>4</sub><sup>2-</sup> (Fig. 4b), constituting the last stage of mineralization process.

### 3.7. Reusability of rGO-Fe<sub>3</sub>O<sub>4</sub>/CB@CF cathode

The stability of the cathode plays a crucial role in practical applications since it determines the reusability of the cathode in several runs without loss of activity. The reusability of the rGO-Fe<sub>3</sub>O<sub>4</sub>/CB@CF cathode was evaluated by repetitive experiments for mineralization of BSF (Fig. 5). The electrode was gently rinsed with ultra-pure water and reused for the next cycle with identical conditions. The catalytic efficiency of the prepared cathode showed less than 4% reduction in terms of TOC removal after 3-h treatment for all five cycles, which shows the oxidation ability of multifunctional heterogeneous cathode and its advantage of avoiding iron leaching and therefore sludge formation. This result indicates that the rGO-Fe<sub>3</sub>O<sub>4</sub>/CB@CF cathode has great reusability and good stability at natural pH in consecutive operation conditions.

Dissolved iron leached from the rGO-Fe<sub>3</sub>O<sub>4</sub>/CB@CF cathode was also investigated by ICP-MS analysis. Throughout the experiment at 500 mA ( $31.25 \text{ mA cm}^{-2}$ ) for 2 h, Fe in dissolved form was found negligible (0.06 ppm) which is adequately reasonable to claim that <sup>•</sup>OH production

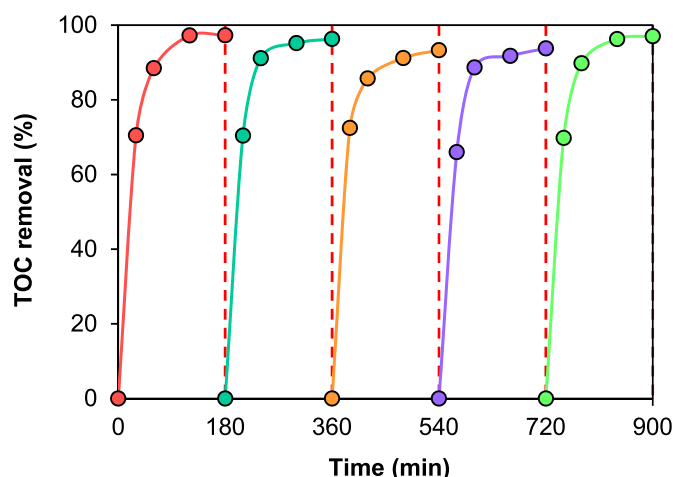


**Fig. 5.** Reusability of rGO-Fe<sub>3</sub>O<sub>4</sub>/CB@CF cathode for the TOC decay of BSF solution at natural pH. [BSF] = 0.1 mM, I = 300 mA ( $18.75 \text{ mA cm}^{-2}$ ), [Na<sub>2</sub>SO<sub>4</sub>] = 50 mM, V = 80 mL.

was completely occurred by the interaction of H<sub>2</sub>O<sub>2</sub> with surface ≡Fe<sup>II</sup> and ≡Fe<sup>III</sup> sites.

## 4. Conclusions

This study showed great ability of heterogeneous EF for efficient oxidation/mineralization of the cytostatic agent BSF. Excellent mineralization rate of BSF solutions was attained at 4 h electrolysis with 500 mA ( $31.25 \text{ mA cm}^{-2}$ ) applied current for all configurations. It was verified that heterogeneous EF with modified cathodes and catalysts improved the mineralization of organic pollutants and widen the working pH range. Five cycle experiments proved that notable performance of heterogeneous EF with rGO-Fe<sub>3</sub>O<sub>4</sub>/CB@CF cathode for organic removal was achieved at natural pH of the solution with great stability. rGO-Fe<sub>3</sub>O<sub>4</sub>/CB@CF cathode played multiple roles in the heterogeneous EF process, it accelerated the ORR process to form the electro-generated H<sub>2</sub>O<sub>2</sub>, while activated the H<sub>2</sub>O<sub>2</sub> simultaneously to form the <sup>•</sup>OH by means of heterogeneous EF process on its surface. Three heterogeneous EF configurations studied in this work provide three benefits over its homogeneous counterpart which could be a promising technique for the cost-effective and sustainable treatment: i) reusable cathode and catalyst, ii) ability to operate at natural pH, iii) improved cathodic properties leading to higher oxygen reduction activity.

Formation and evolution of carboxylic acids and aromatic intermediates were also assessed and based on identified intermediate products, a plausible mineralization pathway was proposed.

### Credit author statement

Ş ule Camcıoğlu: Conceptualization, Investigation, Methodology, Draft preparation, Writing, Formal analysis; Baran Özyurt: Conceptualization, Investigation, Validation, Writing; Nihal Oturan: Supervision, Methodology, Formal analysis, Validation; David Portehault: Investigation, Formal analysis; Clement Trelu: Supervision, Validation; Mehmet A. OTURAN: Supervision, Resources, Writing – review & editing, Project administration

### Declaration of competing interest

The authors declare that they have no known competing financial interests or personal relationships that could have appeared to influence the work reported in this paper.

### Data availability

Data will be made available on request.

### Acknowledgments

Sule Camcioglu and Baran Ozyurt acknowledge TUBITAK (The Scientific and Technological Research Council of Turkey) for providing financial support through 2219-International Postdoctoral Research Fellowship Program for Turkish Citizens. Sule Camcioglu and Baran Ozyurt thank both Ankara University and Gustave Eiffel University for their support of their postdoctoral research.

### References

Barhoumi, N., Olvera-Vargas, H., Oturan, N., Huguenot, D., Gadri, A., Ammar, S., Brillas, E., Oturan, M.A., 2017. Kinetics of oxidative degradation/mineralization pathways of the antibiotic tetracycline by the novel heterogeneous electro-Fenton process with solid catalyst chalcocopyrite. *Appl. Catal. B Environ.* 209, 637–647. <https://doi.org/10.1016/j.apcatb.2017.03.034>.

Barhoumi, N., Oturan, N., Olvera-Vargas, H., Brillas, E., Gadri, A., Ammar, S., Oturan, M. A., 2016. Pyrite as a sustainable catalyst in electro-Fenton process for improving oxidation of sulfamethazine. *Kinetics, mechanism and toxicity assessment. Water Res.* 94, 52–61. <https://doi.org/10.1016/j.watres.2016.02.042>.

Barıŝçı, S., Turkay, O., Ulusoy, E., Őeker, M.G., Yüksel, E., Dimoglo, A., 2018. Electro-oxidation of cytostatic drugs: experimental and theoretical identification of by-products and evaluation of ecotoxicological effects. *Chem. Eng. J.* 334, 1820–1827. <https://doi.org/10.1016/j.cej.2017.11.105>.

Berhe, R.N., Kassahun, S.K., Kang, J.W., Verma, M., Kim, H., 2022. Synthesis of Fe<sub>3</sub>O<sub>4</sub>/CNT/ACF cathode-based electro-fenton system for efficient mineralization of methylene blue dye: kinetics and mechanism. *J. Environ. Chem. Eng.* 10, 108672 <https://doi.org/10.1016/j.jece.2022.108672>.

Bhuvaneshwari, S., Pratheeksha, P.M., Anandan, S., Rangappa, D., Gopalan, R., Rao, T.N., 2014. Efficient reduced graphene oxide grafted porous Fe<sub>3</sub>O<sub>4</sub> composite as a high performance anode material for Li-ion batteries. *Phys. Chem. Chem. Phys.* 16, 5284–5294. <https://doi.org/10.1039/C3CP54778G>.

Brillas, E., 2022. Progress of homogeneous and heterogeneous electro-Fenton treatments of antibiotics in synthetic and real wastewaters. A critical review on the period 2017–2021. *Sci. Total Environ.* 153102 <https://doi.org/10.1016/j.scitotenv.2022.153102>.

Brillas, E., Martínez-Huitle, C.A., 2015. Decontamination of wastewaters containing synthetic organic dyes by electrochemical methods. An updated review. *Appl. Catal. B Environ.* 166, 603–643. <https://doi.org/10.1016/j.apcatb.2014.11.016>.

Brillas, E., Sirés, I., Oturan, M.A., 2009. Electro-Fenton process and related electrochemical technologies based on fenton's reaction chemistry. *Chem. Rev.* 109, 6570–6631. <https://doi.org/10.1021/cr900136g>.

Burgos-Castillo, R.C., Sirés, I., Sillanpää, M., Brillas, E., 2018. Application of electrochemical advanced oxidation to bisphenol A degradation in water. Effect of

chemosphere.2017.12.014.

Calza, P., Medana, C., Sarro, M., Rosato, V., Agiotti, R., Baiocchi, C., Minero, C., 2014. Photocatalytic degradation of selected anticancer drugs and identification of their transformation products in water by liquid chromatography–high resolution mass spectrometry. *J. Chromatogr. A* 1362, 135–144. <https://doi.org/10.1016/j.chroma.2014.08.035>.

Camcioglu, S., Özyurt, B., Oturan, N., Trelu, C., Oturan, M.A., 2022. Fast and complete destruction of the anti-cancer drug cytarabine from water by electrocatalytic oxidation using electro-fenton process. *Catalysts* 12, 1598. <https://doi.org/10.3390/catal12121598>.

Cavalcante, R.P., da Rocha Sandim, L., Bogo, D., Barbosa, A.M.J., Osugi, M.E., Blanco, M., de Oliveira, S.C., de Fatima Cepa Matos, M., Machulek, A., Ferreira, V.S., 2013. Application of Fenton, photo-Fenton, solar photo-Fenton, and UV/H<sub>2</sub>O<sub>2</sub> to degradation of the antineoplastic agent mitoxantrone and toxicological evaluation. *Environ. Sci. Pollut. Res.* 20, 2352–2361. <https://doi.org/10.1007/s11356-012-1110-y>.

Chen, H., Zhang, Z., Yang, Z., Yang, Q., Li, B., Bai, Z., 2015. Heterogeneous fenton-like catalytic degradation of 2, 4-dichlorophenoxyacetic acid in water with FeS. *Chem.Eng. J.* 273, 481–489. <https://doi.org/10.1016/j.cej.2015.03.079>.

Chen, L., Xie, J., Huang, L., Gong, X., 2023. Iron oxide anchored on porous carbon derived from metal–organic frameworks as an efficient catalyst toward in situ generation of H<sub>2</sub>O<sub>2</sub> and a hydroxyl radical for methylene blue degradation in microbial fuel cells. *Energy Fuel.* 37, 5469–5477. <https://doi.org/10.1021/acs.energyfuels.2c04185>.

Chen, W., Yang, X., Huang, J., Zhu, Y., Zhou, Y., Yao, Y., Li, C., 2016. Iron oxide containing graphene/carbon nanotube based carbon aerogel as an efficient E-Fenton cathode for the degradation of methyl blue. *Electrochim. Acta* 200, 75–83. <https://doi.org/10.1016/j.electacta.2016.03.044>.

Çıplak, Z., Yıldız, A., Yıldız, N., 2020. Green preparation of ternary reduced graphene oxide-au@ polyaniline nanocomposite for supercapacitor application. *J. Energy Storage* 32, 101846. <https://doi.org/10.1016/j.est.2020.101846>.

Cleveland, V., Bingham, J.-P., Kan, E., 2014. Heterogeneous Fenton degradation of bisphenol A by carbon nanotube-supported Fe<sub>3</sub>O<sub>4</sub>. *Sep. Purif. Technol.* 133, 388–395. <https://doi.org/10.1016/j.seppur.2014.06.061>.

Coria, G., Pérez, T., Siés, I., Brillas, E., Nava, J.L., 2018. Abatement of the antibiotic levofloxacin in a solar photoelectro-Fenton flow plant: modeling the dissolved organic carbon concentration-time relationship. *Chemosphere* 198, 174–181. <https://doi.org/10.1016/j.chemosphere.2018.01.112>.

Cui, L., Huang, H., Ding, P., Zhu, S., Jing, W., Gu, X., 2020. Cogeneration of H<sub>2</sub>O<sub>2</sub> and OH via a novel Fe<sub>3</sub>O<sub>4</sub>/MWCNTs composite cathode in a dual-compartment electro-Fenton membrane reactor. *Sep. Purif. Technol.* 237, 116380 <https://doi.org/10.1016/j.seppur.2019.116380>.

Cui, L., Li, Z., Li, Q., Chen, M., Jing, W., Gu, X., 2021. Cu/CuFe<sub>2</sub>O<sub>4</sub> integrated graphite felt as a stable bifunctional cathode for high-performance heterogeneous electro-Fenton oxidation. *Chem. Eng. J.* 420, 127666 <https://doi.org/10.1016/j.cej.2020.127666>.

Dang, Y., Bai, Y., Zhang, Y., Yang, X., Sun, X., Yu, S., Zhou, Y., 2022. Tannic acid reinforced electro-Fenton system based on GO-Fe<sub>3</sub>O<sub>4</sub>/NF cathode for the efficient catalytic degradation of PNP. *Chemosphere* 289, 133046. <https://doi.org/10.1016/j.chemosphere.2021.133046>.

Deng, F., Olvera-Vargas, H., Zhou, M., Qiu, S., Siés, I., Brillas, E., 2023. Critical review on the mechanisms of Fe<sup>+</sup> regeneration in the electro-fenton process: fundamentals and boosting strategies. *Chem. Rev.* 123, 4635–4662. <https://doi.org/10.1021/acs.chemrev.2c00684>.

Deng, J., Wen, X., Wang, Q., 2012. Solvothermal in situ synthesis of Fe<sub>3</sub>O<sub>4</sub>-multi-walled carbon nanotubes with enhanced heterogeneous Fenton-like activity. *Mater. Res. Bull.* 47, 3369–3376. <https://doi.org/10.1016/j.materresbull.2012.07.021>.

Diaw, P.A., Oturan, N., Seye, M.D.G., Mbaye, O.M.A., Mbaye, M., Coly, A., Aaron, J.-J., Oturan, M.A., 2020. Removal of the herbicide monolinuron from waters by the electro-Fenton treatment. *J. Electroanal. Chem.* 864, 114087 <https://doi.org/10.1016/j.jelechem.2020.114087>.

Divyapriya, G., Nidheesh, P.V., 2020. Importance of graphene in the electro-Fenton process. *ACS Omega* 5, 4725–4732. <https://doi.org/10.1021/acsomega.9b04201>.

Dong, H., Zhang, X., Han, Yu, Hongbing, Yu, 2018. Graphene-doped carbon black gas diffusion electrode for nonmetallic electrochemical advanced oxidation process under mild conditions. *Environ. Technol.* 39, 2959–2966. <https://doi.org/10.1080/09593330.2017.1370022>.

Dos Santos, A.J., Siés, I., Alves, A.P.M., Martínez-Huitle, C.A., Brillas, E., 2020. Vermiculite as heterogeneous catalyst in electrochemical Fenton-based processes: application to the oxidation of Ponceau SS dye. *Chemosphere* 240, 124838. <https://doi.org/10.1016/j.chemosphere.2019.124838>.

Dos Santos, A.J., Siés, I., Brillas, E., 2021. Removal of bisphenol A from acidic sulfate medium and urban wastewater using persulfate activated with electroregenerated Fe<sup>2+</sup>. *Chemosphere* 263, 128271. <https://doi.org/10.1016/j.chemosphere.2020.128271>.

Du, X., Oturan, M.A., Zhou, M., Belkessa, N., Su, P., Cai, J., Trelu, C., Mousset, E., 2021. Nanostructured electrodes for electrocatalytic advanced oxidation processes: from materials preparation to mechanisms understanding and wastewater treatment applications. *Appl. Catal. B Environ.* 296, 120332 <https://doi.org/10.1016/j.apcatb.2021.120332>.

Es' haghzade, Z., Pajootan, E., Bahrami, H., Arami, M., 2017. Facile synthesis of Fe<sub>3</sub>O<sub>4</sub> nanoparticles via aqueous based electro chemical route for heterogeneous electro-Fenton removal of azo dyes. *J. Taiwan Inst. Chem. Eng.* 71, 91–105. <https://doi.org/10.1016/j.jtice.2016.11.015>.

- Feit, P.W., Rastrup-Andersen, N., 1973. 4-Methanesulfonyloxybutanol: hydrolysis of busulfan. *J. Pharmaceut. Sci.* 62, 1007–1008. <https://doi.org/10.1002/jps.2600620634>.
- Feng, L., Song, W., Oturan, N., Karbasi, M., van Hullebusch, E.D., Esposito, G., Giannakis, S., Oturan, M.A., 2023. Electrochemical oxidation of Naproxen in aqueous matrices: elucidating the intermediates' eco-toxicity, by assessing its degradation pathways via experimental and density functional theory (DFT) approaches. *Chem. Eng. J.* 451, 138483 <https://doi.org/10.1016/j.cej.2022.138483>.
- Ganiyu, S.O., Martínez-Huitle, C.A., 2019. Nature, mechanisms and reactivity of electrogenerated reactive species at thin-film boron-doped diamond (BDD) electrodes during electrochemical wastewater treatment. *Chemelectrochem* 6, 2379–2392. <https://doi.org/10.1002/celec.201900159>.
- Ganiyu, S.O., Nidheesh, P.V., Oturan, M.A., 2022. Synthesis and application of nanostructured iron oxides heterogeneous catalysts for environmental applications. In: *Advanced Materials for Sustainable Environmental Remediation*. Elsevier, pp. 583–608. <https://doi.org/10.1016/B978-0-323-90485-8.00014-X>.
- Ganiyu, S.O., Zhou, M., Martínez-Huitle, C.A., 2018. Heterogeneous electro-Fenton and photoelectro-Fenton processes: a critical review of fundamental principles and application for water/wastewater treatment. *Appl. Catal. B Environ.* 235, 103–129. <https://doi.org/10.1016/j.apcatb.2018.04.044>.
- Gao, L., Zhuang, J., Nie, L., Zhang, J., Zhang, Y., Gu, N., Wang, T., Feng, J., Yang, D., Perrett, S., 2007. Intrinsic peroxidase-like activity of ferromagnetic nanoparticles. *Nat. Nanotechnol.* 2, 577–583. <https://doi.org/10.1038/nnano.2007.260>.
- García-Segura, S., Brillas, E., 2011. Mineralization of the recalcitrant oxalic and oxamic acids by electrochemical advanced oxidation processes using a boron-doped diamond anode. *Water Res.* 45, 2975–2984. <https://doi.org/10.1016/j.watres.2011.03.017>.
- Gerardino, H.C.L., Freitas, T.K.F.S., Manholer, D.D., França, F., Oliveira, J.H., Noldestem, E.A., Lima, A.R.F., Bertotti, M., Giroto, E.M., Garcia, J.C., 2020. Electrochemical generation of H<sub>2</sub>O<sub>2</sub> using gas diffusion electrode improved with rGO intensified with the Fe<sub>3</sub>O<sub>4</sub>/GO catalyst for degradation of textile wastewater. *J. Water Process Eng.* 36, 101377 <https://doi.org/10.1016/j.jpwe.2020.101377>.
- González-Burciaga, L.A., García-Prieto, J.C., García-Roig, M., Lares-Asef, I., Núñez-Núñez, C.M., Proal-Nájera, J.B., 2021. Cytostatic drug 6-mercaptopurine degradation on pilot scale reactors by advanced oxidation processes: UV-C/H<sub>2</sub>O<sub>2</sub> and UV-C/TiO<sub>2</sub>/H<sub>2</sub>O<sub>2</sub> kinetics. *Catalysts* 11, 567. <https://doi.org/10.3390/catal11050567>.
- González-Burciaga, L.A., Núñez-Núñez, C.M., Proal-Nájera, J.B., 2022. Challenges of TiO<sub>2</sub> heterogeneous photocatalysis on cytosstatic compounds degradation: state of the art. *Environ. Sci. Pollut. Res.* 29, 42251–42274. <https://doi.org/10.1007/s11356-021-17241-8>.
- Gopinath, A., Pisharody, L., Popat, A., Nidheesh, P.V., 2022. Supported catalysts for heterogeneous electro-Fenton processes: recent trends and future directions. *Curr. Opin. Solid State Mater. Sci.* 26, 100981 <https://doi.org/10.1016/j.cossms.2022.100981>.
- Gormez, F., Gormez, Ö., Gözmen, B., Kalderis, D., 2019. Degradation of chloramphenicol and metronidazole by electro-Fenton process using graphene oxide-Fe<sub>3</sub>O<sub>4</sub> as heterogeneous catalyst. *J. Environ. Chem. Eng.* 7, 102990 <https://doi.org/10.1016/j.jece.2019.102990>.
- Governo, M., Santos, M.S.F., Alves, A., Madeira, L.M., 2017. Degradation of the cytosstatic 5-Fluorouracil in water by Fenton and photo-assisted oxidation processes. *Environ. Sci. Pollut. Res.* 24, 844–854. <https://doi.org/10.1007/s11356-016-7827-2>.
- Hien, S.A., Trelu, C., Oturan, N., Assémian, A.S., Briton, B.G.H., Drogui, P., Adouby, K., Oturan, M.A., 2022. Comparison of homogeneous and heterogeneous electrochemical advanced oxidation processes for treatment of textile industry wastewater. *J. Hazard Mater.* 129326 <https://doi.org/10.1016/j.jhazmat.2022.129326>.
- Huot, M., Poinson, V., Mercier, L., Valade, C., Desmaris, R., Lemare, F., Paci, A., 2013. Physico-chemical stability of busulfan in injectable solutions in various administration packages. *Drugs R* 13, 87–94. <https://doi.org/10.1007/s40268-013-0003-y>.
- Hu, X., Liu, B., Deng, Y., Chen, H., Luo, S., Sun, C., Yang, P., Yang, S., 2011. Adsorption and heterogeneous Fenton degradation of 17 $\alpha$ -methyltestosterone on nano Fe<sub>3</sub>O<sub>4</sub>/MWCNTs in aqueous solution. *Appl. Catal. B Environ.* 107, 274–283. <https://doi.org/10.1016/j.apcatb.2011.07.025>.
- Hua, Z., Ma, W., Bai, X., Feng, R., Yu, L., Zhang, X., Dai, Z., 2014. Heterogeneous Fenton degradation of bisphenol A catalyzed by efficient adsorptive Fe<sub>3</sub>O<sub>4</sub>/GO nanocomposites. *Environ. Sci. Pollut. Res.* 21, 7737–7745. <https://doi.org/10.1007/s11356-014-2728-8>.
- Ioannou-Tfofa, L., Fatta-Kassinos, D., 2020. Cytostatic drug residues in wastewater treatment plants: sources, removal efficiencies and current challenges. *Fate Eff. Anticancer Drugs Environ.* 103–138 [https://doi.org/10.1007/978-3-030-21048-9\\_6](https://doi.org/10.1007/978-3-030-21048-9_6).
- Kanjil, M.I., Muneer, M., Abdelhaleem, A., Chu, W., 2020. Degradation of methotrexate by UV/peroxymonosulfate: kinetics, effect of operational parameters and mechanism. *Chin. J. Chem. Eng.* 28, 2658–2667. <https://doi.org/10.1016/j.cjche.2020.05.033>.
- Kavinkumar, T., Sastikumar, D., Manivannan, S., 2015. Effect of functional groups on dielectric, optical gas sensing properties of graphene oxide and reduced graphene oxide at room temperature. *RSC Adv.* 5, 10816–10825. <https://doi.org/10.1039/C4RA12766H>.
- Khan, M.A.M., Khan, W., Ahamed, M., Alhazaa, A.N., 2019. Investigation on the structure and physical properties of Fe<sub>3</sub>O<sub>4</sub>/RGO nanocomposites and their photocatalytic application. *Mater. Sci. Semicond. Process.* 99, 44–53. <https://doi.org/10.1016/j.mssp.2019.04.005>.
- Kocijan, M., Čurković, L., Radošević, T., Podlogar, M., 2021. Enhanced photocatalytic activity of hybrid rGO@TiO<sub>2</sub>/CN nanocomposite for organic pollutant degradation under solar light irradiation. *Catalysts* 11, 1023. <https://doi.org/10.3390/catal11091023>.
- Kosjek, T., Negreira, N., Heath, E., de Alda, M.L., Barceč, D., 2018. Aerobic activated sludge transformation of vincristine and identification of the transformation products. *Sci. Total Environ.* 610, 892–904. <https://doi.org/10.1016/j.scitotenv.2017.08.061>.
- Kulaksız, E., Kayan, B., Gözmen, B., Kalderis, D., Oturan, N., Oturan, M.A., 2022. Comparative degradation of 5-fluorouracil in aqueous solution by using H<sub>2</sub>O<sub>2</sub>-modified subcritical water, photocatalytic oxidation and electro-Fenton processes. *Environ. Res.* 204, 111898 <https://doi.org/10.1016/j.envres.2021.111898>.
- Le, T.X.H., Bechelany, M., Lacour, S., Oturan, N., Oturan, M.A., Cretin, M., 2015. High removal efficiency of dye pollutants by electron-Fenton process using a graphene based cathode. *Carbon N. Y.* 94, 1003–1011. <https://doi.org/10.1016/j.carbon.2015.07.086>.
- Li, J., Ai, Z., Zhang, L., 2009. Design of a neutral electro-Fenton system with Fe@Fe<sub>2</sub>O<sub>3</sub>/ACF composite cathode for wastewater treatment. *J. Hazard Mater.* 164, 18–25. <https://doi.org/10.1016/j.jhazmat.2008.07.109>.
- Li, S., Gong, Y., Yang, Y., He, C., Hu, L., Zhu, L., Sun, L., Shu, D., 2015. Recyclable CNTs/Fe<sub>3</sub>O<sub>4</sub> magnetic nanocomposites as adsorbents to remove bisphenol A from water and their regeneration. *Chem. Eng. J.* 260, 231–239. <https://doi.org/10.1016/j.cej.2014.09.032>.
- Li, W., Nanaboina, V., Chen, F., Korshin, G.V., 2016. Removal of polycyclic synthetic musks and antineoplastic drugs in ozonated wastewater: quantitation based on the data of differential spectroscopy. *J. Hazard Mater.* 304, 242–250. <https://doi.org/10.1016/j.jhazmat.2015.10.035>.
- Lin, H., Oturan, N., Wu, J., Zhang, H., Oturan, M.A., 2017. Cold incineration of sucralose in aqueous solution by electro-Fenton process. *Sep. Purif. Technol.* 173, 218–225. <https://doi.org/10.1016/j.seppur.2016.09.028>.
- Lutterbeck, C.A., Baginska, E., Machado, É.L., Kümmerer, K., 2015. Removal of the anti-cancer drug methotrexate from water by advanced oxidation processes: aerobic biodegradation and toxicity studies after treatment. *Chemosphere* 141, 290–296. <https://doi.org/10.1016/j.chemosphere.2015.07.069>.
- Marquez, A.A., Siñés, I., Brillas, E., Nava, J.L., 2020. Mineralization of Methyl Orange azo dye by processes based on H<sub>2</sub>O<sub>2</sub> electrogeneration at a 3D-like air-diffusion cathode. *Chemosphere* 259, 127466. <https://doi.org/10.1016/j.chemosphere.2020.127466>.
- Martínez-Huitle, C.A., Einaga, Y., Oturan, M.A., 2022. Conductive-synthetic diamond materials in meeting the sustainable development goals. *Curr. Opin. Solid State Mater. Sci.* 26, 101019 <https://doi.org/10.1016/j.cossms.2022.101019>.
- Martínez-Huitle, C.A., Rodrigo, M.A., Siñés, I., Scialdone, O., 2023. A critical review on latest innovations and future challenges of electrochemical technology for the abatement of organics in water. *Appl. Catal. B Environ.* 328, 122430 <https://doi.org/10.1016/j.apcatb.2023.122430>.
- Mbaye, M., Diaw, P.A., Mbaye, O.M.A., Oturan, N., Seye, M.D.G., Trelu, C., Coly, A., Tine, A., Aaron, J.-J., Oturan, M.A., 2022. Rapid removal of fungicide thiram in aqueous medium by electro-Fenton process with Pt and BDD anodes. *Sep. Purif. Technol.* 281, 119837 <https://doi.org/10.1016/j.seppur.2021.119837>.
- Moratalla, Á., Lacasa, E., Cañizares, P., Rodrigo, M.A., Sáez, C., 2022. Electro-Fenton-based technologies for selectively degrading antibiotics in aqueous media. *Catalysts* 12, 602. <https://doi.org/10.3390/catal12060602>.
- Munoz, M., de Pedro, Z.M., Casas, J.A., Rodriguez, J.J., 2015. Preparation of magnetite-based catalysts and their application in heterogeneous Fenton oxidation—a review. *Appl. Catal. B Environ.* 176, 249–265. <https://doi.org/10.1016/j.apcatb.2015.04.003>.
- Murrieta, M.F., Siñés, I., Brillas, E., Nava, J.L., 2020. Mineralization of Acid Red 1 azo dye by solar photoelectro-Fenton-like process using electrogenerated HClO and photogenerated Fe(II). *Chemosphere* 246, 125697. <https://doi.org/10.1016/j.chemosphere.2019.125697>.
- Muzenda, C., Arotiba, O.A., 2022. Improved magnetite nanoparticle immobilization on a carbon felt cathode in the heterogeneous electro-fenton degradation of aspirin in wastewater. *ACS Omega* 7, 19261–19269. <https://doi.org/10.1021/acsomega.2c00627>.
- Myers, A.L., Kawedia, J.D., Champlin, R.E., Kramer, M.A., Nieto, Y., Ghose, R., Andersson, B.S., 2017. Clarifying busulfan metabolism and drug interactions to support new therapeutic drug monitoring strategies: a comprehensive review. *Expet Opin. Drug Metabol. Toxicol.* 13, 901–923. <https://doi.org/10.1080/17425255.2017.1360277>.
- Nidheesh, P.V., Ganiyu, S.O., Martínez-Huitle, C.A., Mousset, E., Olvera-Vargas, H., Trelu, C., Zhou, M., Oturan, M.A., 2023a. Recent advances in electro-Fenton process and its emerging applications. *Crit. Rev. Environ. Sci. Technol.* 53, 887–913. <https://doi.org/10.1080/10643389.2022.2093074>.
- Nidheesh, P.V., Ganiyu, S.O., Martínez-Huitle, C.A., Mousset, E., Olvera-Vargas, H., Trelu, C., Zhou, M., Oturan, M.A., 2022. Recent advances in electro-Fenton process and its emerging applications. *Crit. Rev. Environ. Sci. Technol.* 1–27. <https://doi.org/10.1080/10643389.2022.2093074>.
- Nidheesh, P.V., Trelu, C., Vargas, H.O., Mousset, E., Ganiyu, S.O., Oturan, M.A., 2023b. Electro-Fenton process in combination with other advanced oxidation processes: challenges and opportunities. *Curr. Opin. Electrochem.* 37, 101171 <https://doi.org/10.1016/j.coelec.2022.101171>.
- Olvera-Vargas, H., Wang, Z., Xu, J., Lefebvre, O., 2022. Synergistic degradation of GenX (hexafluoropropylene oxide dimer acid) by pairing graphene-coated Ni-foam and boron doped diamond electrodes. *Chem. Eng. J.* 430, 132686 <https://doi.org/10.1016/j.cej.2021.132686>.
- Oturan, N., Ganiyu, S.O., Raffy, S., Oturan, M.A., 2017. Sub-stoichiometric titanium oxide as a new anode material for electro-Fenton process: application to electrocatalytic destruction of antibiotic amoxicillin. *Appl. Catal. B Environ.* 217, 214–223. <https://doi.org/10.1016/j.apcatb.2017.05.062>.

- Pieczynska, A., Fiszka Borzyszkowska, A., Ofiarska, A., Siedlecka, E.M., 2017. Removal of cytostatic drugs by AOPs: a review of applied processes in the context of green technology. *Crit. Rev. Environ. Sci. Technol.* 47, 1282–1335. <https://doi.org/10.1080/10643389.2017.1370990>.
- Poza-Nogueiras, V., Rosales, E., Pazos, M., Sanroman, M.A., 2018. Current advances and trends in electro-Fenton process using heterogeneous catalysts—a review. *Chemosphere* 201, 399–416. <https://doi.org/10.1016/j.chemosphere.2018.03.002>.
- Radat, A., Drygała, A., Hawelek, L., Łukowiec, D., 2017. Structure and optical properties of Fe<sub>3</sub>O<sub>4</sub> nanoparticles synthesized by co-precipitation method with different organic modifiers. *Mater. Char.* 131, 148–156. <https://doi.org/10.1016/j.matchar.2017.06.034>.
- Roig, B., Marqueten, B., Delpla, I., Bessonneau, V., Sellier, A., Leder, C., Thomas, O., Bolek, R., Kummerer, K., 2014. Monitoring of methotrexate chlorination in water. *Water Res.* 57, 67–75. <https://doi.org/10.1016/j.watres.2014.03.008>.
- Rusevova, K., Kopinke, F.-D., Georgi, A., 2012. Nano-sized magnetic iron oxides as catalysts for heterogeneous Fenton-like reactions—influence of Fe (II)/Fe (III) ratio on catalytic performance. *J. Hazard Mater.* 241, 433–440. <https://doi.org/10.1016/j.jhazmat.2012.09.068>.
- Sadeghi, M., Mehdinejad, M.H., Mengelizadeh, N., Mahdavi, Y., Pourzamani, H., Hajizadeh, Y., Zare, M.R., 2019. Degradation of diclofenac by heterogeneous electro-Fenton process using magnetic single-walled carbon nanotubes as a catalyst. *J. Water Process Eng.* 31, 100852. <https://doi.org/10.1016/j.jwpe.2019.100852>.
- Saiphanendra, B., Saxena, T., Singh, S.A., Madras, G., Srivastava, C., 2017. Synergistic effect of co-existence of hematite (α-Fe<sub>2</sub>O<sub>3</sub>) and magnetite (Fe<sub>3</sub>O<sub>4</sub>) nanoparticles on graphene sheet for dye adsorption. *J. Environ. Chem. Eng.* 5, 26–37. <https://doi.org/10.1016/j.jece.2016.11.017>.
- Scaria, J., Nidheesh, P.V., 2022. Magnetite–reduced graphene oxide nanocomposite as an efficient heterogeneous Fenton catalyst for the degradation of tetracycline antibiotics. *Environ. Sci. Water Res. Technol.* 8, 1261–1276. <https://doi.org/10.1039/D2EW00019A>.
- Sheng, Y., Song, S., Wang, X., Song, L., Wang, C., Sun, H., Niu, X., 2011. Electrogeneration of hydrogen peroxide on a novel highly effective acetylene black-PTFE cathode with PTFE film. *Electrochim. Acta* 56, 8651–8656. <https://doi.org/10.1016/j.electacta.2011.07.069>.
- Siedlecka, E.M., 2020. Removal of cytostatic drugs from water and wastewater: progress in the development of advanced treatment methods. *Fate Eff. Anticancer drugs Environ* 197–219. [https://doi.org/10.1007/978-3-030-21048-9\\_9](https://doi.org/10.1007/978-3-030-21048-9_9).
- Siriés, I., Brillas, E., Oturan, M.A., Rodrigo, M.A., Panizza, M., 2014. Electrochemical advanced oxidation processes: today and tomorrow. A review. *Environ. Sci. Pollut. Res.* 21, 8336–8367. <https://doi.org/10.1007/s11356-014-2783-1>.
- Skoglund, C., Bassyouni, F., Abdel-Rehim, M., 2013. Monolithic packed 96-tips set for high-throughput sample preparation: determination of cyclophosphamide and busulfan in whole blood samples by monolithic packed 96-tips and LC-MS. *Biomed. Chromatogr.* 27, 714–719. <https://doi.org/10.1016/j.chroma.2009.10.072>.
- Sopaj, F., Oturan, N., Pinson, J., Podvorica, F., Oturan, M.A., 2016. Effect of the anode materials on the efficiency of the electro-Fenton process for the mineralization of the antibiotic sulfamethazine. *Appl. Catal. B Environ.* 199, 331–341. <https://doi.org/10.1016/j.apcatb.2016.06.035>.
- Sopaj, F., Oturan, N., Pinson, J., Podvorica, F.I., Oturan, M.A., 2020. Effect of cathode material on electro-Fenton process efficiency for electrocatalytic mineralization of the antibiotic sulfamethazine. *Chem. Eng. J.* 384, 331–341. <https://doi.org/10.1016/j.cej.2019.123249>.
- Tang, J., Wang, J., 2017. Fe<sub>3</sub>O<sub>4</sub>-MWCNT magnetic nanocomposites as efficient fenton-like catalysts for degradation of sulfamethazine in aqueous solution. *ChemistrySelect* 2, 10727–10735. <https://doi.org/10.1002/slct.201702249>.
- Tao, L., Ren, H., Yu, F., 2021. High-efficiency electro-catalytic performance of green dill biochar cathode and its application in electro-Fenton process for the degradation of pollutants. *New J. Chem.* 45, 19273–19282. <https://doi.org/10.1039/D1NJ03430H>.
- Wang, K., Li, H., Yang, Y., Wang, P., Zheng, Y., Song, L., 2022. Making cathode composites more efficient for electro-fenton and bio-electro-fenton systems: a review. *Sep. Purif. Technol.* 122302. <https://doi.org/10.1016/j.seppur.2022.122302>.
- Wang, S., Zhao, Y., Gao, M., Xue, H., Xu, Y., Feng, C., Shi, D., Liu, K., Jiao, Q., 2018. Green synthesis of porous cocoon-like rGO for enhanced microwave-absorbing performances. *ACS Appl. Mater. Interfaces* 10, 42865–42874. <https://doi.org/10.1021/acsami.8b15416>.
- Wang, Y., Du, Y., Qiang, R., Tian, C., Xu, P., Han, X., 2016. Interfacially engineered sandwich-like rGO/carbon microspheres/rGO composite as an efficient and durable microwave absorber. *Adv. Mater. Interfac.* 3, 1500684. <https://doi.org/10.1002/admi.201500684>.
- Wang, Yujing, Zhao, G., Chai, S., Zhao, H., Wang, Yanbin, 2013. Three-dimensional homogeneous ferrite-carbon aerogel: one pot fabrication and enhanced electro-Fenton reactivity. *ACS Appl. Mater. Interfaces* 5, 842–852. <https://doi.org/10.1021/am302437a>.
- Wang, Z., Olvera-Vargas, H., Martins, M.V.S., Garcia-Rodriguez, O., Garaj, S., Lefebvre, O., 2023. High performance and durable graphene-grafted cathode for electro-Fenton degradation of tetramethyldecynediol. *Chem. Eng. J.* 455, 140643. <https://doi.org/10.1016/j.cej.2022.140643>.
- Xie, F., Gao, Y., Zhang, Jingbin, Bai, H., Zhang, Jianfeng, Li, Z., Zhu, W., 2022. A novel bifunctional cathode for the generation and activation of H<sub>2</sub>O<sub>2</sub> in electro-Fenton: characteristics and mechanism. *Electrochim. Acta* 430, 141099. <https://doi.org/10.1016/j.electacta.2022.141099>.
- Xu, L., Wang, J., 2012. Fenton-like degradation of 2, 4-dichlorophenol using Fe<sub>3</sub>O<sub>4</sub> magnetic nanoparticles. *Appl. Catal. B Environ.* 123, 117–126. <https://doi.org/10.1016/j.apcatb.2012.04.028>.
- Xu, Z., Gao, H., Guoxin, H., 2011. Solution-based synthesis and characterization of a silver nanoparticle–graphene hybrid film. *Carbon N. Y.* 49, 4731–4738. <https://doi.org/10.1016/j.carbon.2011.06.078>.
- Xue, X., Hanna, K., Deng, N., 2009. Fenton-like oxidation of Rhodamine B in the presence of two types of iron (II, III) oxide. *J. Hazard Mater.* 166, 407–414. <https://doi.org/10.1016/j.apcatb.2012.04.028>.
- Yang, W., Oturan, N., Raffy, S., Zhou, M., Oturan, M.A., 2020a. Electrocatalytic generation of homogeneous and heterogeneous hydroxyl radicals for cold mineralization of anti-cancer drug Imatinib. *Chem. Eng. J.* 383. <https://doi.org/10.1016/j.cej.2019.123155>.
- Yang, W., Zhou, M., Cai, J., Liang, L., Ren, G., Jiang, L., 2017. Ultrahigh yield of hydrogen peroxide on graphite felt cathode modified with electrochemically exfoliated graphene. *J. Mater. Chem. A* 5, 8070–8080. <https://doi.org/10.1039/C7TA01534H>.
- Yang, W., Zhou, M., Oturan, N., Bechelany, M., Cretin, M., Oturan, M.A., 2020b. Highly efficient and stable FeII/FeIII LDH carbon felt cathode for removal of pharmaceutical ofloxacin at neutral pH. *J. Hazard Mater.* 393, 122513. <https://doi.org/10.1016/j.jhazmat.2020.122513>.
- Yang, W., Zhou, M., Oturan, N., Li, Y., Oturan, M.A., 2019. Electrocatalytic destruction of pharmaceutical imatinib by electro-Fenton process with graphene-based cathode. *Electrochim. Acta* 305, 285–294. <https://doi.org/10.1016/j.electacta.2019.03.067>.
- Yu, L., Yang, X., Ye, Y., Wang, D., 2015. Efficient removal of atrazine in water with a Fe 3 O 4/MWCNTs nanocomposite as a heterogeneous Fenton-like catalyst. *RSC Adv.* 5, 46059–46066. <https://doi.org/10.1039/C5RA04249F>.
- Yuan, H., Xu, Y., Jia, H., Zhou, S., 2016. Superparamagnetic Fe 3 O 4/MWCNTs heterostructures for high frequency microwave absorption. *RSC Adv.* 6, 67218–67225. <https://doi.org/10.1039/C6RA11610H>.
- Zhai, L.-F., Sun, M., Guo, H.-Y., Sun, M., 2019. Surface modification of graphite support as an effective strategy to enhance the electro-Fenton activity of Fe<sub>3</sub>O<sub>4</sub>/graphite composites in situ fabricated from acid mine drainage using an air-cathode fuel cell. *ACS Sustain. Chem. Eng.* 7, 8367–8374. <https://doi.org/10.1021/acssuschemeng.9b00008>.
- Zhang, H., Li, Y., Zhao, Y., Li, G., Zhang, F., 2019. Carbon black oxidized by air calcination for enhanced H<sub>2</sub>O<sub>2</sub> generation and effective organics degradation. *ACS Appl. Mater. Interfaces* 11, 27846–27853. <https://doi.org/10.1021/acsaami.9b07765>.
- Zhang, J., Chang, V.W.C., Giannis, A., Wang, J.-Y., 2013. Removal of cytostatic drugs from aquatic environment: a review. *Sci. Total Environ.* 445, 281–298. <https://doi.org/10.1016/j.scitotenv.2012.12.061>.
- Zhang, J., Wang, G., Zhang, L., Fu, X., Liu, Y., 2014. Catalytic oxidative desulfurization of benzothiophene with hydrogen peroxide catalyzed by Fenton-like catalysts. *React. Kinet. Mech. Catal.* 113, 347–360. <https://doi.org/10.1007/s1144-014-0750-y>.
- Zhang, X.-Y., Sun, S.-H., Sun, X.-J., Zhao, Y.-R., Chen, L., Yang, Y., Lü, W., Li, D.-B., 2016. Plasma-induced, nitrogen-doped graphene-based aerogels for high-performance supercapacitors. *Light Sci. Appl.* 5, e16130–e16130. <https://doi.org/10.1038/lsa.2016.130>.
- Zhao, H., Wang, Yujing, Wang, Yanbin, Cao, T., Zhao, G., 2012. Electro-Fenton oxidation of pesticides with a novel Fe<sub>3</sub>O<sub>4</sub>@Fe<sub>2</sub>O<sub>3</sub>/activated carbon aerogel cathode: high activity, wide pH range and catalytic mechanism. *Appl. Catal. B Environ.* 125, 120–127. <https://doi.org/10.1016/j.apcatb.2012.05.044>.
- Zhou, F., Wang, Y., Wu, W., Jing, T., Mei, S., Zhou, Y., 2016. Synergetic signal amplification of multi-walled carbon nanotubes-Fe<sub>3</sub>O<sub>4</sub> hybrid and trimethyloctadecylammonium bromide as a highly sensitive detection platform for tetrabromobisphenol A. *Sci. Rep.* 6, 1–12. <https://doi.org/10.1038/srep38000>.
- Zhou, L., Zhang, H., Ji, L., Shao, Y., Li, Y., 2014. Fe 3 O 4/MWCNT as a heterogeneous Fenton catalyst: degradation pathways of tetrabromobisphenol A. *RSC Adv.* 4, 24900–24908. <https://doi.org/10.1039/C4RA02333A>.
- Zhou, W., Meng, X., Gao, J., Sun, F., Zhao, G., 2021. Janus graphite felt cathode dramatically enhance the H<sub>2</sub>O<sub>2</sub> yield from O<sub>2</sub> electroreduction by the hydrophilicity-hydrophobicity regulation. *Chemosphere* 278, 130382. <https://doi.org/10.1016/j.chemosphere.2021.130382>.
- Zhou, Y., Liu, X., Zhao, Y., Luo, S., Wang, L., Yang, Y., Oturan, M.A., Mu, Y., 2018. Structure-based synergistic mechanism for the degradation of typical antibiotics in electro-Fenton process using Pd–Fe<sub>3</sub>O<sub>4</sub> model catalyst: theoretical and experimental study. *J. Catal.* 365, 184–194. <https://doi.org/10.1016/j.jcat.2018.07.002>.
- Zong, J., 2018. One-pot simplified co-precipitation synthesis of reduced graphene oxide/Fe<sub>3</sub>O<sub>4</sub> composite and its microwave electromagnetic properties. *Mater. Lett.* 106, 22–25. <https://doi.org/10.1016/j.matlet.2013.04.097>.
- Zubir, N.A., Yacou, C., Motuzas, J., Zhang, X., Diniz da Costa, J.C., 2014. Structural and functional investigation of graphene oxide–Fe<sub>3</sub>O<sub>4</sub> nanocomposites for the heterogeneous Fenton-like reaction. *Sci. Rep.* 4, 4594. <https://doi.org/10.1038/srep04594>.
- Zubir, N.A., Yacou, C., Motuzas, J., Zhang, X., Zhao, X.S., da Costa, J.C.D., 2015. The sacrificial role of graphene oxide in stabilising a Fenton-like catalyst GO–Fe 3 O 4. *Chem. Commun.* 51, 9291–9293. <https://doi.org/10.1039/C5CC02922D>.